Carbon Trends 13 (2023) 100316

Contents lists available at ScienceDirect

Carbon Trends

journal homepage: www.elsevier.com/locate/cartre

Activated biochars as sustainable and effective supports for hydrogenations

Somayeh Taghavi [a,b], Elena Ghedini [b], Markus Peurla [c], Giuseppe Cruciani [d], Federica Menegazzo [b], Dmitry Yu. Murzin [e], Michela Signoretto [b,*]

[a] Faculty of Chemistry, University of Mazandaran, Babolsar 47416-95447, Iran
[b] Department of Molecular Sciences and Nanosystems, CATMAT Lab, Ca' Foscari University of Venice and INSTM RUVe, via Torino 155 Mestre, Venezia 30172, Italy
[c] Institute of Biomedicine, University of Turku, Kiinamyllynkatu 10, Turku 20520, Finland
[d] Physics and Earth Sciences Department, University of Ferrara, Via Saragat1, Ferrara 44122, Italy
[e] Johan Gadolin Process Chemistry Centre, Åbo Akademi University, Henriksgatan 2, Turku/Åbo 20500, Finland

ARTICLE INFO

Keywords:
Biomass pyrolysis
Activated biochar
Nickel
Aluminum
Hydrogenation catalyst

ABSTRACT

Activated biochars were obtained from pyrolysis and CO_2-physical activation of four different biomasses including tannery shaving waste (T), vine wood waste (W), barley waste (B) and Sargassum, brown macroalgae of Venice lagoon (A). The potential of obtained carbonaceous materials as the supports of Ni,Al catalysts was investigated in levulinic acid (LA) conversion to γ-valerolactone (GVL) as a model hydrogenation reaction. Al-containing species as the Lewis acid sites for the dehydration step were incorporated to the supports using wet impregnation or precipitation. Ni as a hydrogenation active phase was added to the supports via wet impregnation. Biochar-based supports and catalysts were characterized by AAS, elemental analysis, FTIR, N_2 physisorption, XRD, SEM, EDS, TEM, He-TPD, NH_3-TPD and TPR techniques. The catalysts were tested for LA hydrogenation to GVL in a batch system and aqueous medium. The results showed that Ni supported on activated biochar was not active due to a lack of Lewis acid sites for dehydration. Precipitated Al-containing species on the biochar-based supports demonstrated a better catalytic performance in the reaction compared to impregnated one because of different interactions with the support and Ni species. Among different supports, the activated biochars obtained from T and W acted as the best ones. A higher catalytic efficiency was strongly influenced by the chemical (aromaticity and stability, presence of N,O-doped and functional groups), textural (the porous texture and surface area), and morphological (higher dispersion of active phases) properties of activated biochars obtained from different biomasses with different natures.

1. Introduction

We are witnessing an era of harsh depletion of fossil resources as a traditional natural resource. One of the main reasons of this serious depletion is the linear economy approach generating wastes and subsequent challenges for the climate, environment, and the humans. Therefore, the circular economy concept aiming at the diminishing wastes, emissions, and energy losses is gaining importance [1]. In this aspect, biomass is a promising substitute for fossil-based raw materials in energy and fuel industries producing of chemicals, fuels and materials in several sectors. One of the most applicable processes for valorization of biomass to energy, fuels, chemicals, and materials is pyrolysis, as a thermochemical decomposition of biomass in the absence of oxygen and at high temperature [2]. Biochar, as the byproduct of pyrolysis comprises carbon (C), hydrogen (H), nitrogen (N), oxygen (O), sulfur (S) and ashes with different percentage. The amounts of each element and ashes in biochar are influenced by the origin of initial biomass, the pyrolysis conditions, and each pre- and post-treatment procedure [3]. Through the pyrolysis process, biomass aliphatic and aromatic carbon chains are converted to biochar aromatic carbon which is considered as a non-graphitic/non-graphitizable carbon [4]. Biochar, as a sustainable carbonaceous material with tunable properties has been used in various applications such as energy generation, soil amendment, absorbents, and catalysis which can confirm its efficiency with respect to the principles established for a circular economy [5,6]. Biochar usually has *in situ* self-doped and functionalized groups of nitrogen, oxygen, sulfur, and phosphorus depending on the native heteroatoms content in the original biomass. This can result in promising catalytic activity and also assist a better anchorage and dispersion of the active phase on the carbonaceous support [7]. On the other hand, most of the biochars have

* Corresponding author.
E-mail address: miky@unive.it (M. Signoretto).

https://doi.org/10.1016/j.cartre.2023.100316
Received 25 August 2023; Received in revised form 13 November 2023; Accepted 25 November 2023
Available online 26 November 2023

a non-ordered structure with very a low surface area and weak porosity limiting their utilization in catalytic applications. Several techniques have been investigated for biochar activation to develop its localized order and hierarchical porous structure. Examples are given by physical (with CO_2, steam, O_3) and chemical (with KOH, NaOH, NH_3, K_2CO_3, $ZnCl_2$, HCl and H_2SO_4) activations [8,9].

In this study, we aimed to investigate the possibility of using biochar as a sustainable and active carbon-based support for Ni,Al nanoparticles with a diminished environmental impact and economic concerns for a model platform molecule hydrogenation. Hence, four different biomasses were selected for the preparation of biochar-based supports: (a) leather tannery waste: an industrial waste and from animal derived raw material, classified as the second generation biomass, rich in collagen, and proteins; (b) vine wood waste: a vegetal and agricultural or food waste from second generation biomass, typically lignocellulosic, made of cellulose, hemicellulose, and lignin; (c) barley waste: a vegetal and agricultural or food waste from second generation biomass, typically lignocellulosic, made of cellulose, lignin and arabinoxylans and rich in protein, lipid, fiber, and vitamins; and (d) *Sargassum* brown macroalgae of the Venice lagoon: from third generation biomass, rich in protein, lipid, and carbohydrates. Tannery shaving waste, vine wood waste, and barley waste are the byproducts of important supply chains in Italy [10], and *Sargassum* brown macroalgae has a widespread distribution in Venice Lagoon and in Po River Delta (Northern Adriatic Sea, Italy) causing some environmental damages [11]. Natural activated carbon materials (activated biochars) were obtained from four biomasses pyrolysis and physical activation using CO_2, as an eco-friendly and efficient approach and were used as the supports of bifunctional Ni, Al-based catalysts for levulinic acid (LA) to γ-valerolactone (GVL) conversion as a model hydrogenation reaction.

GVL can be used as a precursor of several other chemicals and as a fuel additive, a green solvent, a perfume ingredient or a food additive [12]. It can be produced from several substrates such as cellulosic carbohydrates, furfural, furfuryl alcohol, LA, and alkyl levulinates [13]. One of the most common and key routes for GVL production is hydrogenation of LA passing from two possible reaction pathways (Scheme 1): (1) LA ketonic group hydrogenation to a very active intermediate, 4-hydroxypentanoic acid, and its simultaneous dehydration passing from an intramolecular esterification and cyclisation giving GVL (Scheme 1, pathway I), and (2) LA dehydration and cyclisation to intermediates α-angelica lactone or β-angelica lactone and their hydrogenation resulting GVL (Scheme 1, pathway II). Overall, each hydrogenation step is catalyzed with active metal catalyst, and each dehydration step proceeds over an acid catalyst or under acidic conditions. One of the possible byproducts of the reaction could be pentatonic acid from subsequence dehydration and hydrogenation of 4-hydroxypentanoic acid in the presence of Brønsted acid sites. Moreover, coke formation is another possible side reaction coming from condensation of LA and especially angelica lactones under severe acidic conditions [14].

Among heterogeneous catalysts for LA conversion to GVL, noble metals such as Ru, Pt, Pd, and Ir, and non-noble metals such as Ni, Cu, Fe, and Mg have been extensively applied as the catalyst's hydrogenation active phase [14–17]. Beside the crucial importance of the active metal phase in LA hydrogenation, a combination of both Lewis and Brønsted acid sites with a proper concentration and dispersion is desired to guarantee and improve the overall performance of the catalyst [18]. In addition, the catalytic supports have a vital influence on the catalytic activity mostly possessing the acid sites for the dehydration step, and catalysts stability affected by coke formation, metal leaching and sintering [19,18]. From the literature, oxide type supports such as ZrO_2, TiO_2, Al_2O_3, SiO_2, MgO, and ZnO, mesoporous silica-based materials such as MCM-41 and SBA-15, microporous zeolites, clays, and carbon-based materials were reported for the target reaction [14,15]. In particular, carbon supported Ru materials and supported Ni catalysts are the most studied catalysts for target model reaction [14–17]. For instance, Cao et al., studied Ru/C and Ru/ZrO@C in both aqueous and acidic mediums and more than 70 % LA conversion and GVL yield were obtained at 140 °C and 10 bar H_2 for 2 h [20]. In addition, N-doped multichambered mesoporous carbon microspheres supported Ni catalysts displayed almost full LA conversion and GVL selectivity [21]. Commercial activated carbon was used as the Ni catalyst support in which 99 % GVL selectivity in 80 % LA conversion was achieved using dioxane as the solvent of reaction at 200 °C and 30 bar H_2, for 4 h [21]. Among utilized supports for both current model reaction and other hydrogenation reactions, carbon-based materials exhibited high surface area, proper porosity, thermal-mechanical stability being suitable for this application. In particular, natural carbon-based materials (biochars) as the solid byproducts of different biomasses pyrolysis could be a highly potential and sustainable carbonaceous support for hydrogenation catalysts. For instance in our previous study [22], leather tannery shaving waste and hazelnut shell have been used as the biomass precursors for preparation of activated biochar supports via pyrolysis and steam-based

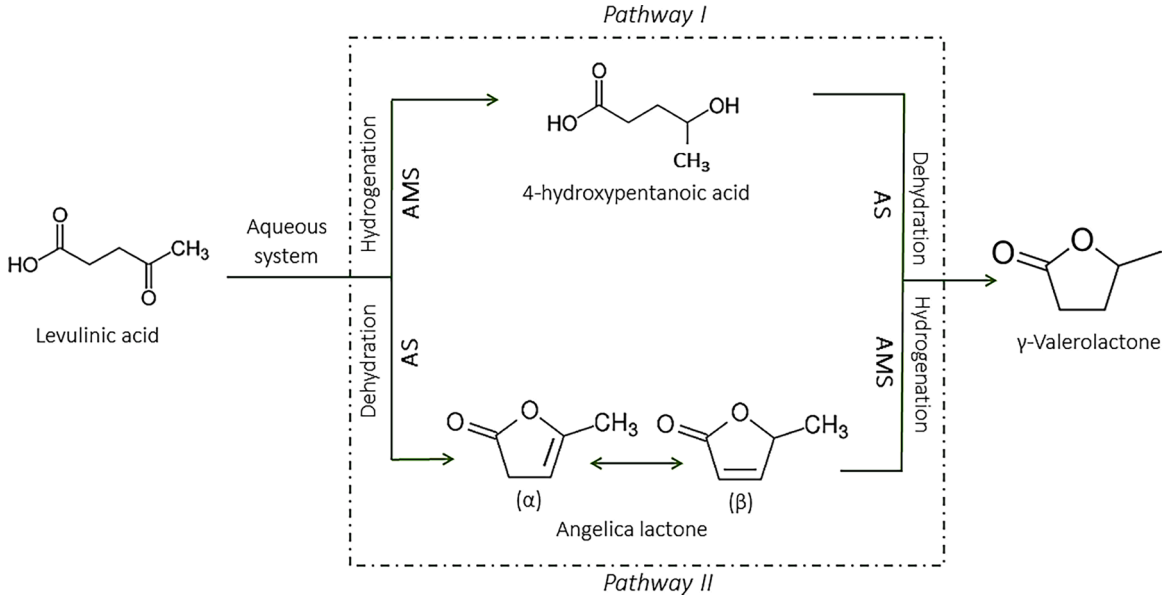

Scheme 1. Possible reaction pathways from levulinic acid to γ-valerolactone (AMS: active metal site; AS: acid site).

physical activation to be used in Ru catalysts. These catalysts were active in selective hydrogenation of 5-hydroxymethylfurfural to 1-hydroxy-2, 5-hexanedione considering the highest performance of the catalyst obtained from hazelnut shells. In another study [23], Pd was incorporated on activated biochar supports obtained from tannery shaving waste, hazelnut shells, rise husks and broken rice grains for benzaldehyde hydrogenation. Rise husks acted as the best biomass for preparation of an efficient support for this model reaction. In addition, activated biochar obtained from tannery shaving waste, barley waste and *Sargassum* brown macroalgae have been successfully used in other non-catalytic applications such as lithium-ion battery [4], lithium-metal free sulphur battery [6], and adsorbent for cationic dyes [24], respectively. To the best of our knowledge, biochars from vine wood waste, barley waste, and leather tannery shaving waste have never been reported as the support of the Ni,Al catalyst for hydrogenation reactions [25].

In the current study, the aim is to investigate the possibility of using activated biochars from different animal and vegetal origins and various generations of biomass as the supports for bifunctional Ni, Al-based catalysts in LA hydrogenation as a model reaction. To achieve this aim, for the first time, activated biochar (obtained from lethaer tannery shaving waste, vine wood waste, barley waste, and *Sargassum* brown macroalgae) were used as the support of Ni, Al for target model hydrogenation reaction. Since activated biochars naturally possess the Brønsted acid functionalities affected by the origin of the initial biomasses, this aspect can be considered as a vital inspiration in formulation of an innovative catalytic system for the bio-based model reactions. Moreover, Al-containing structures as the Lewis acid sites of the catalyst were introduced to the biochar supports by two different impregnation and precipitation techniques, and Ni as hydrogenation active metal was impregnated on the supports. All supports and catalysts were studied by different characterization techniques and their performances were tested in LA to GVL transformation as a model reaction.

2. Experimental

2.1. Support preparation

Four different biomasses were selected for preparation of biochar-based supports: (a) Tannery shaving waste that was obtained from PASUBIO S.p.A. tannery (Arzignano, Italy), provided by GOAST technology, Green Organic Agents for Sustainable Tanneries (LIFE project, LIFE16 ENV/IT/000416); (b) Vine wood waste (W) that was supplied from a cellar in Conegliano, Italy; (c) Barley waste (B) that was provided from Padova, Italy; (d) *Sargassum*, brown macroalgae (A) that was collected in the Venice lagoon.

Before pyrolysis, T biomass was dried in the air for 48 h, while A was washed with tap water and distilled water, dried in the air for 48 h and further dried in the oven at 110 °C for 2 h. On the contrary, W and B were directly used in pyrolysis without any pretreatment. To obtain biochar, the pyrolysis of biomass was performed in a laboratory-scale prototype plant (Carbolite custom model EVT 12/450B) consisting of a vertical oven with a fixed bed tubular quartz reactor. In a pyrolysis run, first, 40 g of a particular biomass (size < 0.250 mm) was charged into the reactor and pyrolyzed at 600 °C, with a heating rate of 5 °C/min, and a residence time of 30 min under N_2 flow of 100 mL/min. Three different products including gas (bio-gas), liquid (bio-oil), and solid (biochar) were obtained from pyrolysis process. In particular, slow pyrolysis was carried out because the aim of the study was obtaining higher mass percentage of biochar (more than 30 % in this study) as the solid product of the pyrolysis [22]. The biochars obtained from pyrolysis step were labeled as B_T, B_W, B_B, and B_A for T, W, B, and A biomasses, respectively. After 30 min of pyrolysis, the temperature was increased to 700 °C with a heating rate of 20 °C/min under N_2 flow of 100 mL/min. Then, the gas was switched to CO_2 as the activation agent with the flow of 100 mL/min and the physical activation was carried out for 4 h. To remove the inorganic residues (ashes), activated biochar was mixed with HCl (Merck, ≥37.0 wt%) (1 M) solution and was sonicated for 1 h. Then, the activated biochar was filtered and washed with deionized water until achieving a neutral pH. The sample was dried in an oven at 110 °C for 12 h. All materials were grinded and sieved to the particle size <180 μm in diameter. The final obtained supports were labeled A_T, A_W, A_B, and A_A, respectively.

2.2. Incorporation of Al as the Lewis acid site

Incorporation of Al via wet impregnation was done in the following way. First a solution of $Al(NO_3)_3{\cdot}9H_2O$ (Sigma-Aldrich, ≥98.0 wt%) in 5 mL deionized water with a proper concentration was prepared to have a final Al loading of 10 wt.%. Second, the desired amount of A_T activated biochar was added to the solution aimed to have a final catalyst weigh of 1.5 g. Then, the mixture was stirred with the rate of 500 rpm, at 25 °C for 1 h. Finally, the solution was evaporated in the oven at 90 °C for 12 h. The final sample of this step was labeled Ali/A_T.

For incorporation of Al via precipitation first, two solutions were prepared: (A) a 50 mL solution of $Al(NO_3)_3.9H_2O$ with a proper concentration to have a final Al loading of 10 wt.%, (B) a solution of NaOH (3 M) (Sigma-Aldrich, ≥98.0 wt%) as the precipitation agent. Then, the solution A and B were added dropwise to a 100 mL mixture of biochar-based support (A_T, A_W, A_B, A_A) in deionized water using a peristaltic pump. Therefore, $Al(OH)_3$ was precipitated on the support keeping the pH of solution in the range of 7, 8 according to the following reaction:

$$Al(NO_3)_3 + 3NaOH \rightarrow Al(OH)_3 + 3NaNO_3$$

Then, the mixture was filtered, washed with distilled water until reaching the neutral pH. Finally, the sample was dried in the oven at 90 °C for 12 h. The final samples of this step were labeled Alp/A_T, Alp/A_W, Alp/A_B, Alp/A_A.

2.3. Introduction of active Ni phase by wet impregnation method

For impregnation of Ni, a solution of $Ni(NO_3)_2{\cdot}6H_2O$ (Merck, 99.999 %) in 5 mL deionized water at the desired concentration was prepared to have a final Ni loading of 10 wt.%. Then, the Al incorporated-activated biochar was added to the solution and the mixture was stirred at 25 °C for 1 h. The solution was evaporated in the oven at 90 °C for 12 h. In addition, a catalyst of A_T supported Ni was prepared following the same approach.

All prepared catalysts were calcined in N_2 with a flow rate of 50 mL/min, at 550 °C, with a heating rate of 5 °C/min, and a residence time of 4 h. After calcination, the catalysts were reduced in the presence of pure H_2 with a flow rate of 50 mL/min, at 400 °C, with a heating rate of 10 °C/min, for 3 h. The prepared catalysts are denoted as Ni/A_T, NiAli/A_T, NiAlp/A_T, NiAlp/A_W, NiAlp/A_B, and NiAlp/A_A.

2.4. Support and catalyst characterizations

The CHNS elemental analyses of biomasses, biochars, and activated biochars were carried out using UNICUBE organic elemental analyzer (Elementar). Then, the amount of inorganic residues (ashes) was measured via the thermo-gravimetric analysis (TGA 8000 PerkinElmer) following the ASTM-D7582 protocol [26] The percentage of oxygen was calculated according to the equation below:

$$O(\%) = 100 - (C\% + H\% + N\% + S\% + ash\%)$$

The Ni content was determined by atomic absorption spectroscopy (AAS) after digestion of the samples (100 mg), using a Perkin-Elmer Analyst (Perkin-Elmer, Waltham, MA, USA) 100 spectrometer.

Fourier transform infrared (FTIR) analyses were performed by Perkin Elmer Spectrum One spectrometer with a wave number range of 400–4000 cm^{-1} and resolution of 4 cm^{-1} at room temperature.

X-ray powder diffraction (XRD) analyses were carried by a Bruker D8

Advance Da Vinci diffractometer equipped with LynxEye detector and a sealed tube providing Cu Kα radiation at an accelerated voltage of 40 kV and an applied current of 30 mA. The determination of the Ni crystallite size was accomplished using the Rietveld method as implemented in the TOPAS v.5 program (Bruker AXS). The crystallite size was calculated as volume-weighted mean column heights based on integral breadths of peaks according to the Double-Voigt approach.

Scanning electron microscopies (SEM) were performed using a Field Emission Gun Electron Scanning Microscope LEO 1525, after metallization with chromium. The images were acquired by In lens detector while the elemental composition was determined using Bruker Quantax EDS.

Transmission electron microscopies (TEM) were performed by JEM-1400Plus, JEOL Ltd with an acceleration voltage of 120 kV and resolution of 0.98 nm using Quemsa II MPix bottom mounted digital camera. A suspension of the gold catalyst in ethanol was applied. TEM images were used to determine the morphology of biochar-based supports, and the distributions of Ni nanoparticles and Al-containing nanostructures on the support.

Specific surface areas and the pore size distributions were evaluated by N_2 adsorption/desorption isotherms at −196 °C using a Tristar II Plus Micromeritics. Micropores and the total surface area were calculated using the t-plot and Langmuir methods, respectively [27]. Micropores volume was calculated by t-plot method. The total pore volume was obtained according to the adsorbed amounts of N_2 at P/P_o values near 0.98.

Temperature-Programmed Desorption under helium (TPD in helium) analyses were carried out using a lab-made equipment to study the presence of oxygenated functional groups on the surface of carbon-based materials. First, 100 mg of the catalyst were charged in a quartz reactor and heated up to 900 °C with the heating rate of 10 °C/min under He flow of 40 mL/min. During heating procedure, the decomposition of oxygenated functional groups occurred by releasing CO and CO_2 gases which were recorded using a thermal conductivity detector (Gow-Mac 24-550 TCD instrument).

NH_3 Temperature-Programmed Desorption (NH_3-TPD) analyses were carried out using a lab-made equipment to study acidity of the catalysts. First, 100 mg of the catalyst were charged in a quartz reactor and degassed in He with a flow rate of 40 mL/min at 500 °C for 90 min. The catalyst was then cooled down to 25 °C prior to adsorption of ammonia. Then, the adsorption of 5 % NH_3/He with a flow rate of 40 mL/min at 25 °C for 30 min was performed. The physisorbed ammonia was removed from the catalyst surface by passing He (40 mL/min) at 25 °C for 30 min. The desorption profiles of NH_3-TPD were recorded using a thermal conductivity detector (Gow-Mac TCD) from 25 to 900 °C at a heating rate of 10 °C/min under the flow of He (40 mL/min).

Temperature-Programmed Reduction (TPR) of the catalysts was performed using a lab-made instrument to study reducibility and the metal-support interactions. First, 100 mg of the sample were charged in a quartz reactor and the sample was heated from 25 °C to 800 °C with a ramp of 10 °C/min under 5 vol% H_2 in Ar with a flow of 40 mL/min. The effluent gases were analyzed by a Micrometrics 2900 analyzer equipped with a TCD detector (Gow-Mac 24–550 TCD instrument).

2.5. Catalytic test

For investigation of the catalytic reactivity, all samples were tested in a batch system namely a stainless-steel autoclave of 400 mL volume. A mechanical stirrer was used and the heating was performed using an electric heater. The autoclave was charged with 50 mL of 0.17 M aqueous solution of levulinic acid, and 400 mg of the catalyst to have a LA/Ni molar ratio of 12.5 : 1. The autoclave was purged ten times with N_2 to remove the air and then was pressurized with 35 bar of H_2. The temperature was increased, and the starting reaction time was considered once the temperature reached the desired value. When the reaction was ended, the autoclave was cooled down to 25 °C and the final mixture was filtered. In addition, the reaction conditions were investigated by changing temperature, H_2 pressure, reaction time, and the LA/catalyst mass ratio.

For analysis of the products, the filtered solution of each reaction was injected to a high-performance liquid chromatography (HPLC) Agilent Technology 1260 Infinity II. An Aminex HPX-87H column was used and the analysis was carried out at column temperature of 57 °C by passing the mobile phase of 5 mM H_2SO_4 with the flow rate of 0.6 mL/min. A UV–vis detector (λ =195 nm) was used for analytes' identification and quantification. The LA conversion (X), GVL yield (Y_{GVL}), carbon balance in liquid phase (CB), and turnover frequency (TOF) were calculated using the following equations:

$$X\ (\%) = \frac{\Delta n}{n_0} \cdot 100$$

$$Y_{GVL}\ (\%) = \frac{n_{GVL}}{n_0} \cdot 100$$

$$CB\ (\%) = \frac{\sum_i (n_{out}) \cdot (C\ atoms)}{(n_0 \cdot C\ atoms\ LA)} \cdot 100$$

$$\mathrm{TOF} = \frac{\Delta n}{\Delta t . n_{Ni}} s^{-1}$$

Where Δn corresponds to the reacted mole of LA during the reaction. n_0, n_{GVL} and n_{out} represent the initial amount of LA, GVL in the final liquid phase, and the content of LA and reaction products in the final liquid phase, respectively. The notation "C atoms" corresponds to the number of carbon atoms in every component. Δt corresponds to the time of the reaction and n_{Ni} is the actual mole of Ni in the catalyst measured by AAS analysis.

3. Results and discussion

3.1. Characterization of biochars

The data of CHNS elemental analysis of biomasses, biochars, and activated biochars are reported in Table 1.

As can be seen, the pyrolysis and activation processes led to an increase of carbon contents and a decrease of H/C ratio in all materials which can be related to carbonization and aromatization phenomena [28]. Exceptionally, activation of B_B to A_B showed an opposite trend which could suggest that activation of this biochar was not complete in the applied conditions.

When comparing different activated biochars, A_W and A_T displayed the highest carbon contents being 82.1 % and 76.7 %, respectively, demonstrating a more aromatic, carbonaceous, and stable structures for catalytic application. Indeed, the heteroatoms distributions of different

Table 1
CHNS elemental analyses of biomasses, biochars, and activated biochars (The amount of elements is reported in mass percentage).

Sample	C [%]	H [%]	N [%]	S [%]	O [%]	Ash [%]	H/C	O/C
T	44.6	6.3	11.5	2.5	N.A[a]	N.A	0.14	–
B_T	73.6	2.7	12.4	0.7	6.1	4.5	0.04	0.08
A_T	76.6	1.1	9.4	0.6	9.8	2.5	0.01	0.13
W	46.6	6.0	0.5	0.2	N.A	N.A	0.13	–
B_W	81.3	1.5	1.1	0.2	8.8	7.1	0.02	0.11
A_W	82.1	0.9	1.3	0.2	13.4	2.1	0.01	0.16
B	49.2	6.7	2.8	0.3	N.A	N.A	0.14	–
B_B	72.8	1.3	5.2	0.2	13.4	7.1	0.02	0.18
A_B	67.0	1.5	4.0	0.2	11.6	15.7	0.02	0.17
A	37.1	5.3	4.8	1.3	N.A	N.A	0.14	–
B_A	43.4	1.2	3.6	2.0	N.A	N.A	0.03	–
A_A	67.1	1.2	6.8	2.8	7.9	14.2	0.02	0.12

[a] N.A: not analyzed.

biochars were affected by the nature of original biomass. The decrease of hydrogen content during pyrolysis and activation is ascribed to the cracking and cleavage of the weak bonds in the biomass and biochar carbonaceous skeletons [29]. In addition, nitrogen, oxygen, and sulfur contents showed different trends in pyrolysis and activation of different biomasses. In every sample, N,O,S heteroatoms could be present as different functional groups or different doped ones in the carbon structure. Indeed, every types of functionality and also doped heteroatom could be connected to the carbon structure or surface with various strength of the covalent bonds. Hence as mentioned above, although carbonization leads to the cleavage of the bonds between heteroatoms and carbons and removal of heteroatoms, it is also highly influenced by the strength of C–N, C–O, S-O bonds in the biomass and biochar structures [30]. Among different activated biochars, A_T, A_A, and A_B exhibited considerable nitrogen contents of 9.4 %, 6.8 % and 4.0 %, respectively, originating from the protein fraction of T, A, and B biomasses. A_W and A_B demonstrated higher oxygen contents and O/C ratios compared to A_T and A_A. A higher oxygen content of activated biochars might be derived from carbohydrate and lignin fractions of lignocellulosic biomasses. The presence of oxygen and nitrogen heteroatoms could suggest more O, N-doped and functional groups in the activated biochar-based supports, being crucial for a better anchorage of the active metal phases in heterogeneous catalysis applications [31]. On the other hand, A_A has a high content of sulfur (2.8 %) compared to others coming from the lipid fraction of algae which might be a serious issue in catalysis since sulfur can poison the noble and non-noble active metals [32–35]. Higher ash fractions of A_B and A_A can be due to the presence of some elements such as Si (Fig. S1) which could not be removed by acid washing [11,36].

Fig. 1(a,b) displays the nitrogen adsorption-desorption isotherms of biochars and activated biochars, respectively. All biochars show an isotherm type III corresponding to non-porous materials according to IUPAC classification (Fig. 1a). A low surface area was obtained for the biochar obtained from pyrolysis of the residual soapberry pericarp at 600 °C [37], while the biochar from pyrolysis of hazelnut shells at 600 °C showed a higher BET surface area of 81 m^2g^{-1} [38]. This confirms that the nature of the initial biomass has a vital impact on the texture or properties of the obtained biochar. Moreover, the low surface area and low porosity of a support could be the issues in catalytic applications especially for a good dispersion of the active phase. Hence, an activation step was applied to improve porosity and the surface area of the biochar-based supports. Four different biochars exhibit different textural behaviors after physical activation procedure being affected by the nature of the initial biomass. In particular, A_A and A_W indicate a combination of type I and type IV isotherms suggesting their hierarchical micro-mesoporous texture (Fig. 1b). The H4 hysteresis loop in the range of $0.4<P/P_o<0.99$ demonstrate narrow slit-shaped pores of the samples.

Moreover, the isotherm of A_T corresponds to a microporous texture

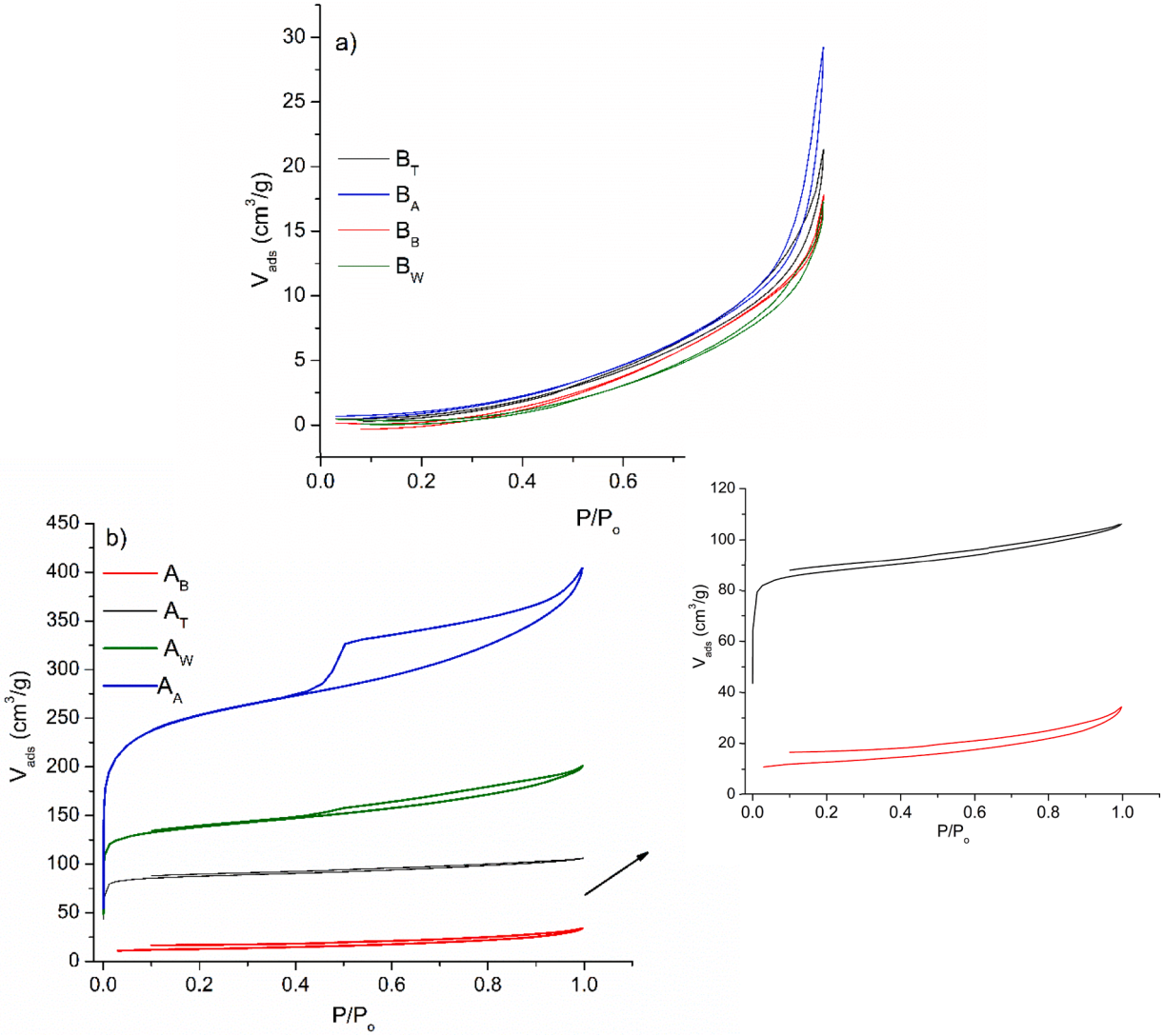

Fig. 1. N_2 adsorption-desorption isotherms of (a) biochars and (b) activated biochars.

(type I) with a narrow hysteresis loop and hence the presence of a small amount of mesopores in this sample. However, the porous texture of A_B did not significantly change by activation. In particular, A_B shows a wide hysteresis loop in the isotherm which can be assigned to the presence of large and elongated pores in the sample. Overall, a higher surface area and porosity of activated biochars suggest their potential and efficiency to be used as supports in heterogenous catalysis.

The functional groups of activated biochars were qualified by FTIR technique. The FTIR spectra of all activated biochars in Fig. 2 display a band at approximately 3400 cm^{-1} demonstrating to the vibrations of O–H functional groups [39]. Higher intensities of these bands for A_T and A_B are related to the vibration of N-containing functional groups namely $–NH_2$ from amines and amides groups originated from the protein fraction of the initial biomasses. The intense band at ca. 1600 cm^{-1} is ascribed to the stretching vibration of aromatic C=C and C=O stretching of conjugated quinones and ketones [40,41] which was confirmed by TPD analysis in helium (Fig. S2). In addition, a series of overlapped bands in the wavenumber range of 1400–900 cm^{-1} can be related to the N,O-doped heteroatoms and functional groups in the skeleton and at the surface of activated biochars such as C–O bonds in alcohols, phenol (confirmed by TPD in Fig. S2), bridging ether between aromatic rings, and N–C and N-COO groups [22]. Furthermore, all activated biochars exhibit the C–H of alkenes at 2850 and 2920 cm^{-1}, and aromatic C–H out of plane vibrations at 800 cm^{-1} [42]. Overall, different activated biochars displayed different FTIR spectra and hence different functionalities which were confirmed by the presence of heteroatoms with different contents in CHNS elemental analysis (Table 1). Such behavior is obviously due to a different natures of the initial biomass.

3.2. Characterization of the catalysts

The AAS results in Table 2 demonstrate that ca. 7, 8 % Ni was actually loaded on the supports. Minor differences of the actual Ni loading in different catalysts might be related to the textural, morphological properties, and chemical functionality of the biochar-based supports which led to a different anchorage and stability of Ni active phase on the support.

From nitrogen adsorption-desorption isotherms displayed in Fig. 3 (a–d), it can be concluded that after introduction of the active sites, the form of isotherms of A_W, and A_A activated biochars remained unchanged, while for A_T sample, a partial change in the form of the hysteresis loop was observed in some cases especially for NiAlp/A_T catalyst. A more prominent change was observed for A_B support after introduction of Al and Ni. NiAlp/A_B exhibited a combination of I and IV isotherm type with H4 hysteresis loop in the range of $0.40<P/P_o<0.99$ demonstrating the presence of micro and mesopores with narrow slit-shaped in this sample.

When comparing the textural properties of activated biochars in Table 2, the surface area and porosity of the samples follow the order of $A_A>A_W>A_T>A_B$. It seems that the biochar from B needed harsher activation conditions for the improvement of textural properties. The surface areas and pore volumes of the catalysts show alterations compared to the supports (Table 2). Particularly, impregnation of only Ni on A_T led to a decrease of the surface area and of the pore volume. In addition, by introduction of both Al and Ni to A_T, A_W and A_B, the surface area and pore volume increased considering the noticeable increment in the case of NiAlp/A_B. On the contrary, introduction of Al and Ni on A_A resulted in

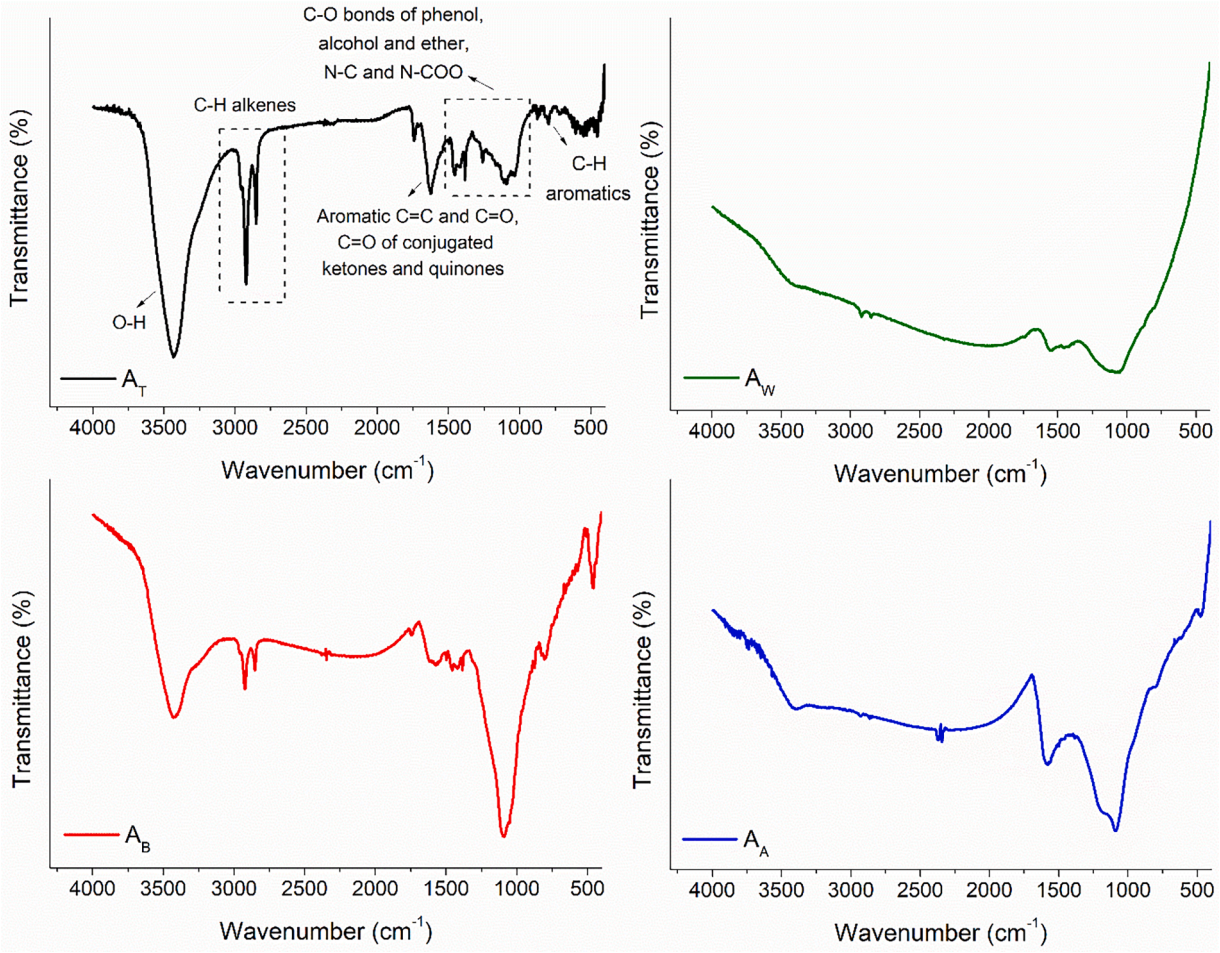

Fig. 2. FTIR spectra of activated biochars.

Table 2
Ni loading (determined by AAS), textural properties (obtained from N_2 physisorption) and Ni,Al crystal size (determinated by XRD) for studied supports and catalysts.

Sample	Ni loading (%)		$S_{Langmuir}$ [a] (m^2g^{-1})	S^b_{micro} (m^2g^{-1})	V^c_{tot} (cm^3g^{-1})	V^d_{micro} (cm^3g^{-1})	Ni crystal size (nm)[e] +/- 0.1 nm	Al crystal size (nm)[e] +/- 0.1 nm
A_T	–	412	356	0.16		0.10	–	–
Ni/A_T	7.5	402	335	0.15		0.09	30	–
$NiAli/A_T$	7.9	529	244	0.22		0.10	12	1.1
$NiAlp/A_T$	7.3	487	401	0.18		0.10	21	1.3
A_W	–	690	571	0.29		0.14	–	–
$NiAlp/A_W$	8.0	726	580	0.30		0.13	17	1.1
A_B	–	79	–	0.04		–	–	–
$NiAlp/A_B$	8.8	445	353	0.17		0.07	27	1.1
A_A	–	1305	905	0.56		0.17	–	–
$NiAlp/A_A$	7.3	1049	719	0.47		0.11	–	–

(a) calculated by Langmuir method, (b) calculated by t-plot method, (c) total pore volume calculated according to the adsorbed amount of N_2 and P/P_o values near 0.98, (d) micropore volume calculated by t-plot method, (e) calculated by Rietveld method.

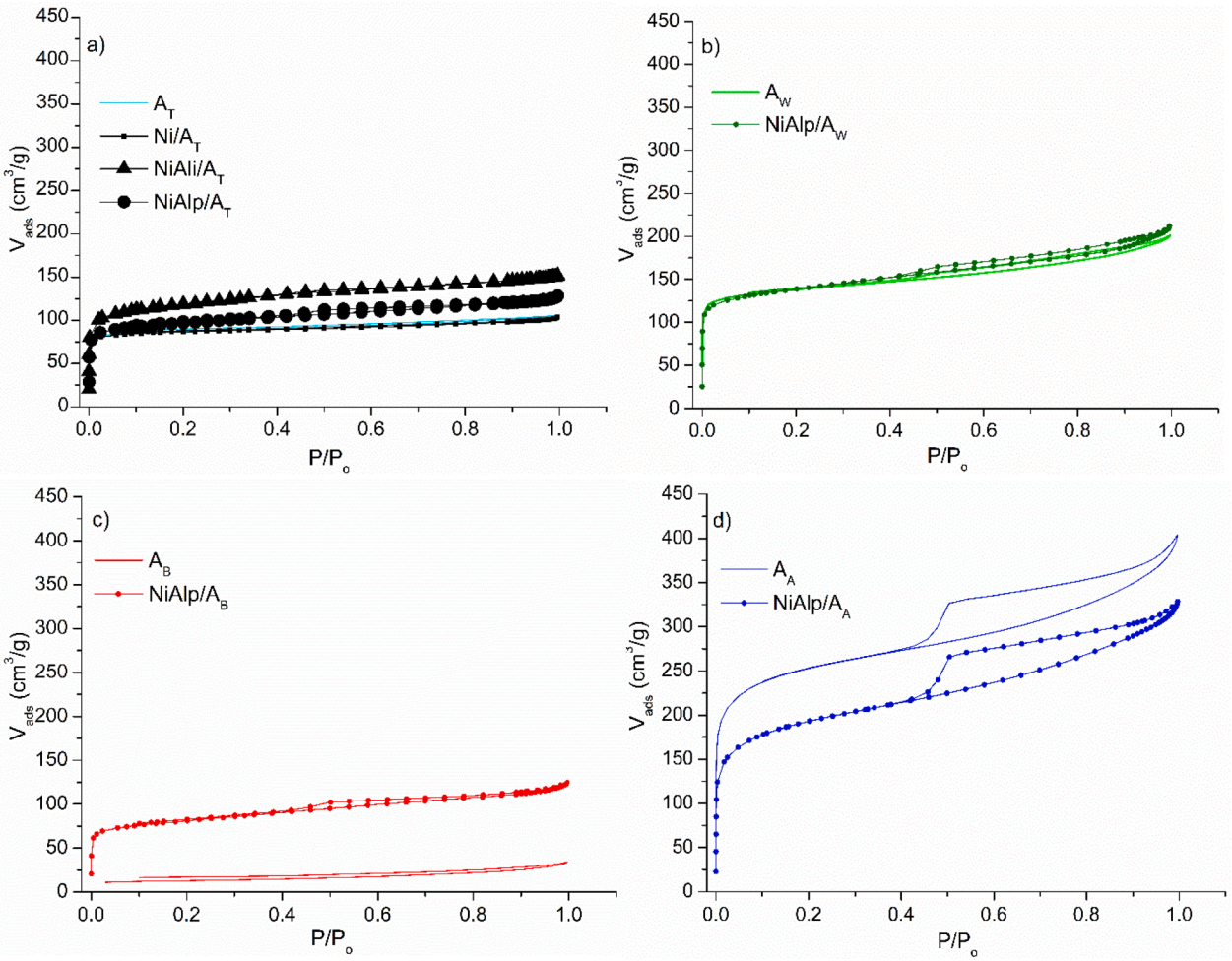

Fig. 3. N_2 adsorption-desorption isotherms of the studied catalysts supported on (a)A_T, (b) A_W, (c) A_B, and (d) A_A.

an opposite trend. As it can be seen in the XRD results of Table 2, the Al crystalline size of all samples is around 1 nm while Ni crystalline size for all samples is higher than 10 nm. Definitely the most pore blockage could be mainly related to agglomerated Ni particles rather than very small Al crystals [43]. In addition, the pore size and shape of every activated biochar support are different and highly significant. A_T is highly microporous and agglomerated Ni particles did not have the possibility to enter the pores and block them. Indeed, looking at the Ni/A_T confirms that the reduction of A_T surface area and pore volume was very slight after impregnation of Ni. This can suggest that most of agglomerated Ni particles stayed on the surface of the catalyst not entered inside the pores. On the other hand, when both Al, and Ni were introduced to the A_T support by both techniques, the surface area increased which can mainly be related to the introduction of Al and interaction of both active sites with the support. This phenomenon was also observed for A_W which was mainly microporous and the texture did not suffer from the entrance of agglomerated Ni particles to the pores and was mainly affected by the interaction of active sites with the support and the surface area increased. However, A_A showed a micro-mesoporous texture and the agglomerated Ni had this possibility

to enter into the mesopores of the support and block them. This could be the reason that pore blockage was more effective in this sample which led to the decrease of surface area after incorporation of active sites. In the case of A_B, the support was almost non porous and the active sites mainly stayed on the surface of the support and had a very strong interaction with support due to the typical chemical structure of this support. Overall for all supports, increase of surface area after incorporation of active site can be explained by: (a) increase of the surface area by introducing alumina, if any, which itself has a developed porosity [44], (b) interactions between the active phases with nitrogen and oxygen doped and functional groups of activated biochars, and inorganic compounds such as silicates in the biochars (Fig. S1) [45,46]. According to the elemental analysis results of Table 1, A_W and A_B samples displayed the highest O/C ratio, while A_B and A_T exhibited a high mass percentage of nitrogen, which suggests the high N,O-doped and functionality in these samples.

The interactions between the active phases and doped and functionalized groups of supports could help in a further activation of the samples by calcination, (d) several studies mentioned the effect of NaOH in removal of the silicate based ashes and subsequent biochar surface area improvement [47,48]. Because NaOH was used as the precipitation agent in this study and the presence of Si was observed in the EDS analyses of A_T and A_B (Fig. S1) of the catalysts, it can be reasonably assumed that NaOH interacted with some of the silicate-based ash in activated biochars according $2NaOH(s) + SiO_2(s) \rightarrow Na_2SiO_3(s) + H_2O$. Na_2SiO_3 formed in this way easily is removed in the water-washing step of the catalysts. Moreover, in A_T and A_B, the amount of ash is high (~15 %) which could explain an increase of the surface area and porosity after introduction of the metal. Therefore, partial Si-leaching from activated biochars during Al precipitation could also improve their surface areas and porosities [47,48].

The XRD patterns of the catalysts are shown in Fig. 4. For all samples, the two broad reflexes at 2θ of ~25° and ~44° can be associated to the (002) and the (100) reflection planes of the carbonaceous material with respect to hexagonal graphite 2H model. The (002) and the (100) reflexes could correspond to the assembling of aromatic ring layers and aromatic molecules extension in every plane of the layer, respectively [4,22]. In the case of NiAli/A_T, two sharp reflexes at 2θ=21° and 27° are ascribed to the crystalline silica contaminations (see Fig. S1a) which were not completely removed in the acid washing step of A_T sample.

For all samples, the lines of Ni° can be observed at 2θ of 44.4°, 51.8°, and 76.4° [49]. It should be noticed that the reflex at 2θ of ~44° overlaps with the line of Ni° crystal which made the (100) reflection planes less visible. In addition, the crystal size of Ni^0 estimated by the Rietveld method (Table 2) was 30 nm, 12 nm, and 21 nm for Ni/A_T, NiAli/A_T, and NiAlp/A_T catalysts, respectively. The difference is due to the presence of Al and its different incorporation methods. In addition, NiAlp/A_W and NiAlp/A_B exhibited Ni crystal size of 17 nm and 27, respectively. This can suggest that the nature and properties of biochar more exactly the surface area and pore size had also a strong effect on the Ni crystal size. Comparing three different catalysts that were prepared with similar method meaning NiAlp/A_T, NiAlp/A_W, NiAlp/A_B can confirm that the higher is the support surface area, the smaller the Ni crystal size.

Two bumps at 2θ ca. 38° and 65° originate from Al crystals addition to the system. These broad and weak peaks might be attributed to the highly dispersed Al on the biochar and the small size of Al crystal (Table 2) in all catalysts [50]. Indeed, it can be predicted that the size and dispersion of Al-containing structures could have a significant influence on the acidic properties of the catalyst and hence its performance in the target reaction. In addition, the activity and selectivity can be affected by the Ni° crystal and particle sizes [51,52]. The results for Ni/A_T, NiAli/A_T, and NiAlp/A_T confirm that the presence of Al and its incorporation method affected the Ni° crystal size and nickel distribution across the support.

The SEM images of NiAli/A_T, NiAlp/A_T, NiAlp/A_W, and NiAlp/A_B are presented in Fig. 5(a–d), respectively, to study the surface morphologies of the catalysts.

The surface morphologies of the catalysts derived from different biochar-based supports varies. NiAli/A_T and NiAlp/A_T display more flat surfaces with some superficial porosities in macro sizes. It can be assumed that most of the superficial pores in A_T-based catalysts are in

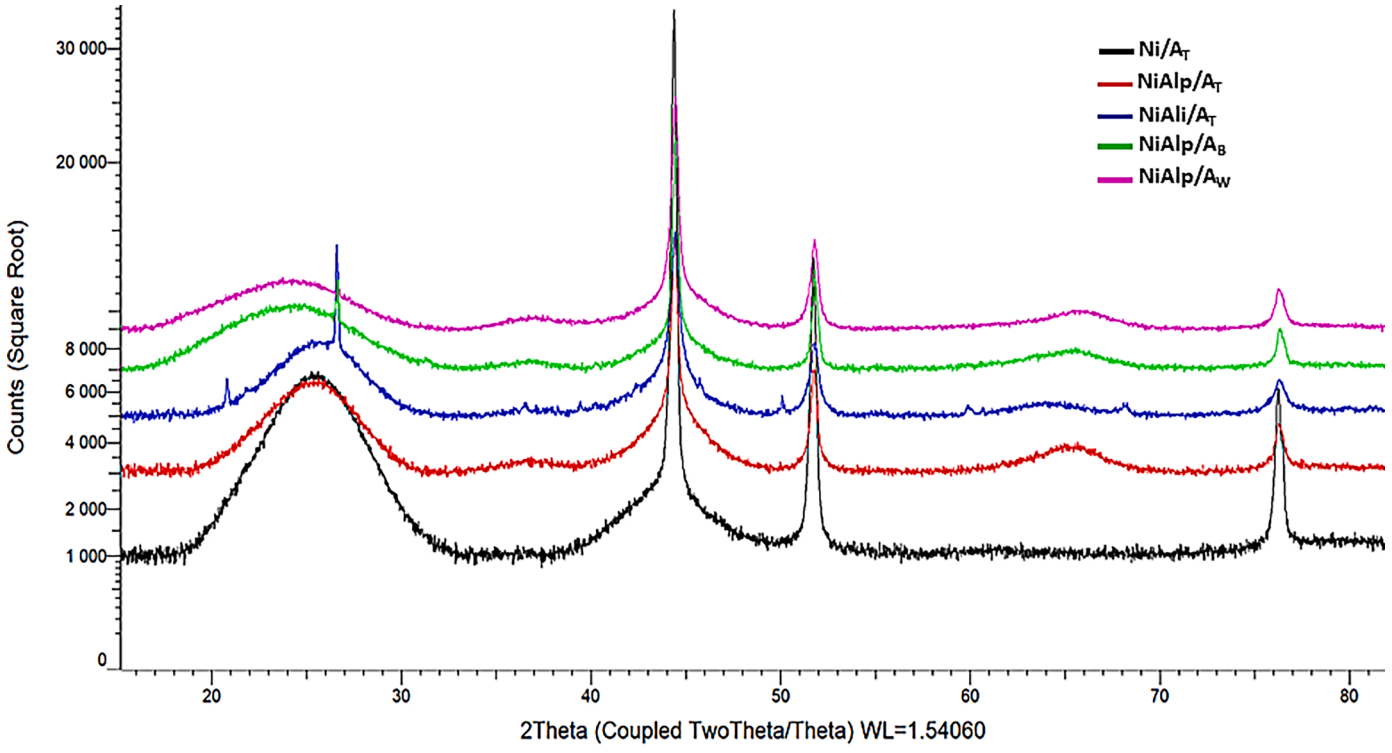

Fig. 4. XRD patterns of the catalysts (form bottom to top: Ni/A_T, NiAlp/A_T, NiAli/A_T, NiAlp/A_B, NiAlp/A_W).

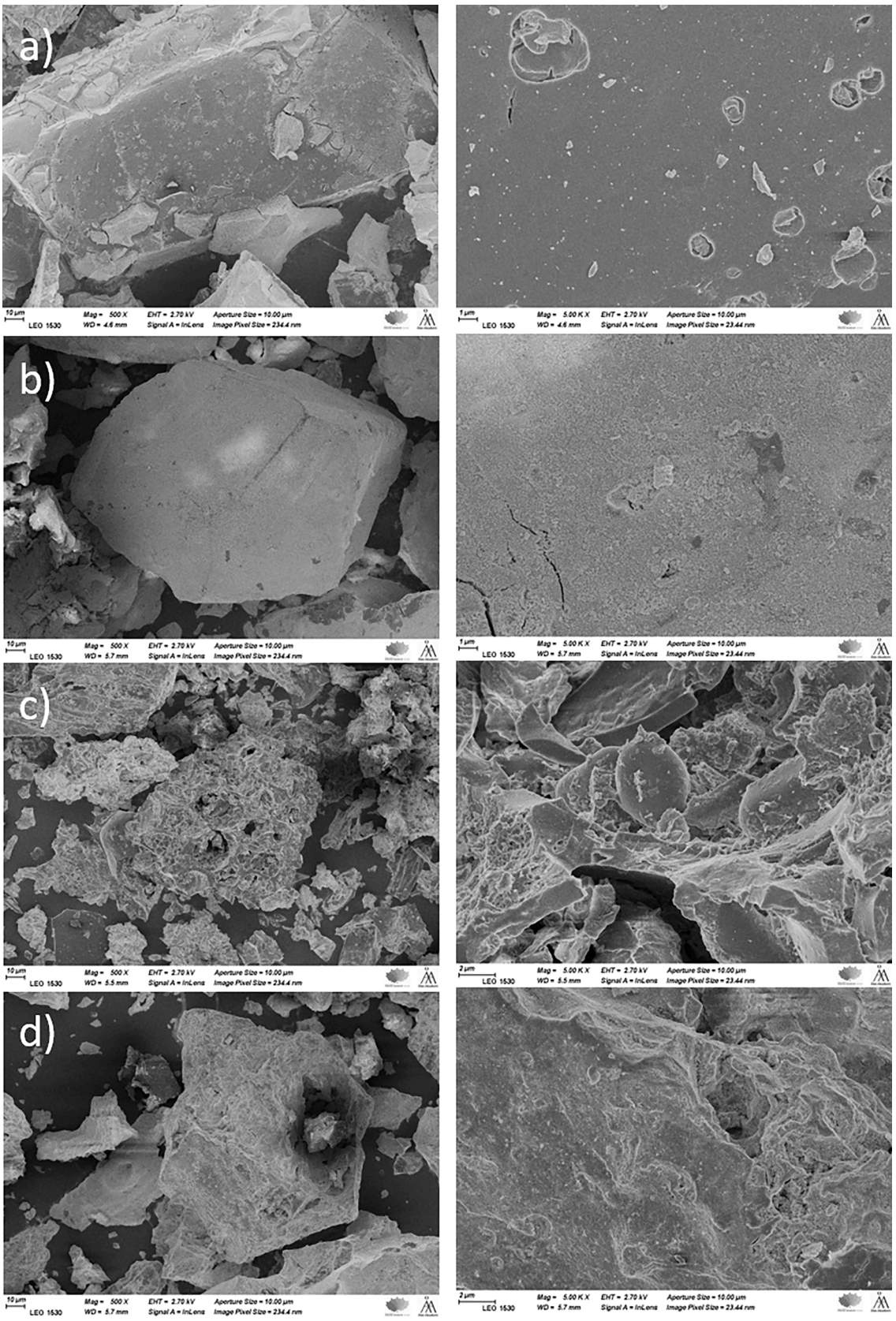

Fig. 5. The SEM images of (a) NiAli/A_T, (b)NiAlp/A_T, (c) NiAlp/A_W, and (d) NiAlp/A_B catalysts, with 500X and 5.00 K X magnifications.

micro and *meso* sizes as it was demonstrated from N_2 physisorption results in Table 2, not being however, visible in SEM images because of the magnification [23]. On the contrary, NiAlp/A_W and NiAlp/A_B have rougher morphologies with irregular surfaces. From the SEM images of NiAlp/A_W (Fig. 5c), the original wood structure is partially visible containing various types of visible porosities such as holes, pits, cavities resulted from the activation procedure which can be confirmed by N_2 adsorption desorption isotherms of the sample in Fig. 3b. Moreover, the surface morphology of NiAlp/A_W was similar to those of the previous studies [53,54]. NiAlp/A_B possesses a rigid, uneven surface with few holes, and *meso* and macropores (Fig. 5d). Indeed, the isotherm of A_B in Fig. 1b confirmed the presence of large and elongated pores in this sample. Moreover, dispersion of the active phases on the supports can be observed from the elemental maps of the catalysts in Fig. S3.

TEM images of NiAlp/A_W and NiAlp/A_B in Fig. 6 confirm that dispersion of the active sites in the catalysts was affected by the surface area and porosity of the supports. In NiAlp/A_W, a higher surface area and porous texture of A_W resulted in highly dispersed active sites, while the active sites in NiAlp/A_B catalyst underwent sintering and agglomeration due to a low surface area and low porosity of A_B. Indeed, a smaller size and a higher dispersion of the active sites could be significant to have a high surface active sites accessibility.

Reducibility of the catalysts was studied by TPR with the profiles displayed in Fig. 7. Generally, all catalysts exhibit two main reduction peaks, below 450 °C, which vary with the extent of interactions between NiO and activated biochar supports with different nature and properties, and the catalysts preparation method. In particular, the reduction peak below 300 °C for NiAlp/A_W could be due to the reduction of bulk NiO having very weak interactions with the support. For all catalysts except NiAlp/A_W, the reduction peak between 300 °C and 450 °C can be ascribed to the medium strength interactions of the Ni species with the supports [46]. The peaks at the temperature above 450 °C suggest the reduction of NiO with strong Ni-support interactions [46,55,56]. Moreover, the peaks at the temperature higher than 500 °C might be due to methanation of activated biochars by hydrogen spillover, and the interactions of their surface functional groups with H_2 [22]. Comparing different catalysts, NiAlp/A_W showed the lowest reduction temperatures and hence the weakest Ni-support interactions. This means that NiO was less stabilized on the A_W support which had the lowest amount of N and O according to elemental analysis (Table 1) and hence the lowest surface functional groups according to FTIR results (Fig. 2). The reduction temperatures of the other catalysts followed the order of NiAlp/A_A>NiAlp/A_T>NiAlp/A_B. Therefore, the presence of more O, N, S-containing functional groups on the activated biochars from different origins (Figs. 2 and S2) led to better interactions of Ni species with the support, their higher stabilization and more difficult reduction. When comparing NiAlp/A_T with NiAli/A_T, the two reduction peaks of NiAlp/A_T appeared at slightly higher temperatures because of different interactions of NiO with the support. It seems that the catalyst obtained by precipitation favors strong interactions of NiO with the support.

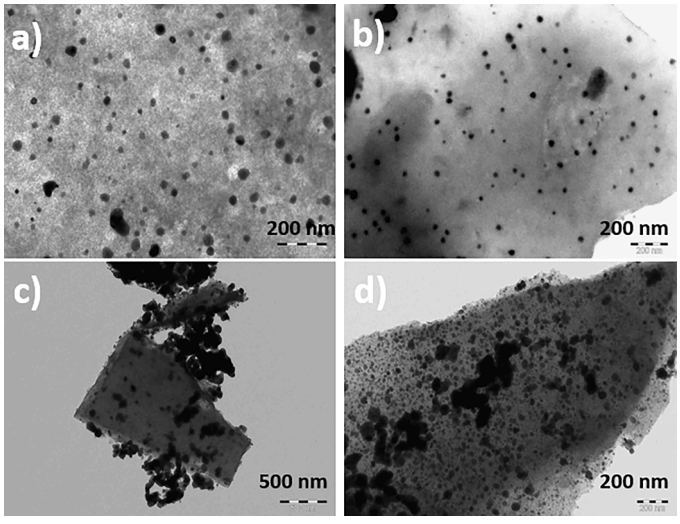

Fig. 6. TEM images of (a,b) NiAlp/A_W and (c,d) NiAlp/A_B catalysts.

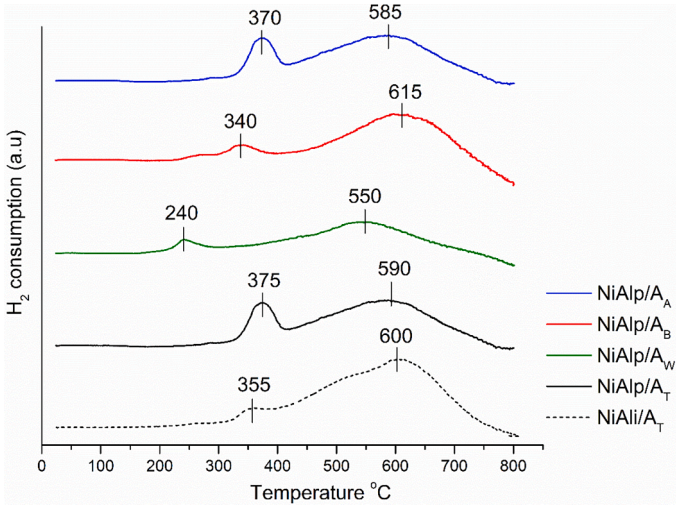

Fig. 7. H_2-TPR profiles of the catalysts.

The presence of acid sites on the surface of the supports and catalysts weas studied by NH_3-TPD the profiles of NiAli/A_T, NiAlp/A_T, A_W, and NiAlp/A_W presented in Fig. 8. In NH_3-TPD profiles, three desorption zones at various temperatures reflect the strength of acid sites. The desorption peaks at the temperature ranges of 50–300 °C, 300–600 °C, and above 600 °C correspond to the weak, moderate and strong Brønsted/Lewis acid sites, respectively [57]. Both A_T and A_W supports exhibited weak, moderate and strong acid sites due to the presence of –COOH and –OH groups which were also observed in FTIR and TPD in He results in Fig. 2 and Fig. S2, respectively. In all samples, Al incorporation contributed to the new acid sites formation on the supports. In the case of A_T sample, presence of aluminum containing species improved weak and strong acid sites of the support considering higher increments of these types of acid sites in NiAlpA_T and NiAli/A_T, respectively. It can be confirmed that addition of Al to the A_T support could provide Lewis acidity in the final catalysts which might have different distributions and hence diverse interactions and strength depending on the aluminum incorporation methods. On the other hand, precipitated Al on A_W led to an enhancement of weak and strong acid sites and creation of new moderate acid sites.

3.3. The effect of Al introduction on the catalytic performance

The performance of synthesized Ni/A_T, NiAli/A_T, and NiAlp/A_T in the transformations of LA to GVL was investigated in a batch reactor in the aqueous medium (Fig. 9). It is noted that all Single Ni, NiAli and NiAlp were introduced to four different supports of this study and tested in the target reaction in which the same trend was obtained. Therefore, only the result of A_T support as the best one is reported. Over Ni/A_T, LA was only slightly converted (11 %) without any GVL production, whereas bifunctional catalysts were active in the proposed reaction. This can confirm that Ni alone was not able to catalyze LA hydrogenation through pathway I (Scheme 1). Therefore, the catalyst of this study was active in the pathway II and we can reasonably assume that Al as Lewis acid sites were needed to first dehydrate LA to angelica lactone followed by a hydrogenation step to GVL over Ni site. Indeed, NH_3-TPD profiles demonstrated the improvement of acid sites of the A_T based catalysts after introduction of Al (Fig. 8). Therefore, the supports can have a vital influence on the activity mostly possessing the acid sites for the

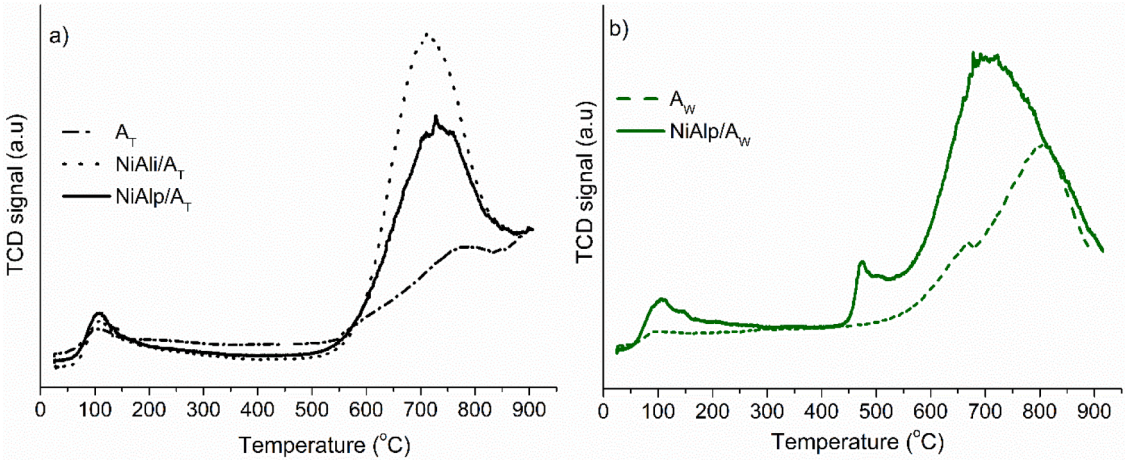

Fig. 8. NH_3-TPD profiles of (a) A_T, NiAli/A_T, NiAlp/A_T, and (b) A_W, NiAlp/A_W samples.

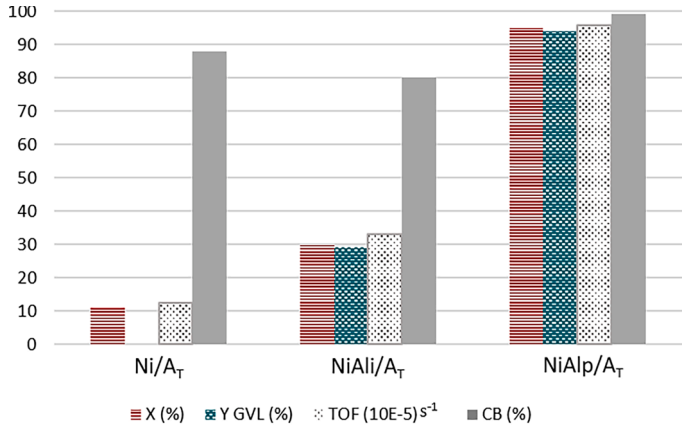

Fig. 9. Transformation of LA to GVL over Ni/A_T, NiAli/A_T, and NiAlp/A_T catalysts. Reaction conditions: 200 °C, 35 bar H_2, 4 h, 0.17 M LA, 400 mg catalyst, 50 ml H_2O. The relative error of HPLC analysis was generally less than ± 5 %.

dehydration step, and catalysts stability affected by coke formation, metal leaching and sintering [18,58,59]. For instance, when Ni-Cu/Al_2O_3 was investigated as the catalyst of the reaction, 96 % yield of GVL at full LA conversion was obtained at harsher reaction conditions of 250 °C, 65 bar H_2 for 2 h [16].

When comparing two catalysts with two Al introduction approaches namely NiAli/A_T and NiAlp/A_T, a higher activity was achieved with the catalyst with precipitated Al giving 95 % LA conversion, 94 % GVL yield and TOF of 96.10^{-5} s^{-1}. Although NiAli/A_T showed a higher amount of strong acid sites compared to NiAlp/A_T (Fig. 8a), we assume that weak acid sites were more active in catalyzing dehydration step which was more significant in the case of NiAlp/A_T. Indeed, these differences in acidic properties of the catalysts are due to different synthesis approaches for Al incorporation in the catalysts. It can be confirmed that precipitation technique resulted in different interactions of Al-containing particles with the supports, their higher dispersion, and hence a surface needed for dehydration. Kumar et al. observed that Lewis acid sites are responsible for dehydration of LA to angelica lactones and Brønsted acid site is prone to ring opening of GVL and formation of valeric acid and hydrocarbons [60]. López and co-workers reported that strong acid sites can catalyze the formation of organic carbonaceous deposits such as humins and fast catalyst deactivation of the catalyst [61]. Additionally, the Ni° crystal size of NiAlp/A_T catalyst (21 nm) was larger than of NiAli/A_T (12 nm) (Table 2), but it seems that the activity of the catalyst in this case was more affected by the acidic properties. Hence, Al precipitation as a better method was applied for other activated biochars support and the effect of type of supports on the catalytic activities will be discussed in the next section.

3.4. The effect of activated biochar supports on the catalytic performance

The performances of different activated biochars as the supports in the catalytic transformation of LA to GVL is demonstrated in Fig. 10. A negligible activity was observed over NiAlp/A_A which might be related to a high amount of sulfur in A_A support revealed by the elemental analysis (Table 1). Several studies demonstrated that sulfur could have a poisoning effect, block Ni active sites in the catalyst, and hinder its activity [52,62,33]. Moreover, activity of NiAlp/A_B was not so high giving 27 % GVL yield and TOF of 43 × 10^{-5} s^{-1} in 42 % LA conversion. The mediocre activity of this catalyst is due to a low surface area and porosity of A_B support (Fig. 1b and Table 2). This led to a low dispersion of Al-containing particles and Ni active sites, their sintering and agglomeration (Fig. 3), and hence low active phases dispersion.

NiAlp/A_T and NiAlp/A_W showed almost the same and the highest activity giving around 95 % LA conversion and GVL yield, 99 % CB and TOF of ca. 95 × 10^{-5} s^{-1}. Highest carbon content of A_T and A_W supports (Table 1) compared to other materials could assist a more aromatic, carbonaceous, and stable structure of the catalysts. In addition, higher oxygen and nitrogen contents in A_T (Table 1) correspond to the presences of more O,N-doped and functionalized groups (Fig. 2) and a better anchorage and stability of active sites on the support. Considering the textural aspect, both NiAlp/A_T and NiAlp/A_W showed high surface areas

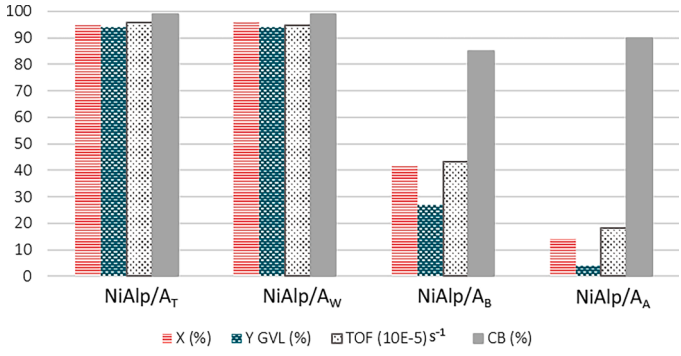

Fig. 10. Transformations of LA to GVL over NiAlp/A_T, NiAlp/A_W, NiAlp/A_B, and NiAlp/A_A catalysts. Reaction conditions: 200 °C, 35 bar H_2, 4 h, 0.17 M LA, 400 mg catalyst, 50 ml H_2O. The relative error of HPLC analysis was generally less than ± 5 %.

and adequate porosities (Fig. 3 and Table 2) compared to NiAlp/A_B being appropriate for a better dispersion of active phases on the support. Moreover, the porous surface of NiAlp/A_W in SEM image (Fig. 5), the high dispersion of active phase in NiAlp/A_W according to TEM image (Fig. 6), smaller Ni° crystals size in NiAlp/A_T and NiAlp/A_W compared to NiAlp/A_B according to XRD (Fig. 4 and Table 2) could be the vital morphological reasons for higher activity of the catalysts. Hengst and co-workers investigated the effect of different methods including wet impregnation, flam spray pyrolysis, precipitation with NaOH, and precipitation with urea for the preparation of Ni/Al_2O_3 catalysts to achieve a smaller Ni particle size with a higher dispersion. Among them, wet impregnation led to a more suitable Ni particle size (6 nm) and dispersion and a higher catalytic activity giving LA conversion of 90 % and GVL yield of 75 % in the aqueous medium at 200 °C, 50 bar H_2, for 4 h [51]. In the current work, several chemical, textural, and morphological factors guaranteed the high activities of NiAlp/A_T and NiAlp/A_W catalysts. In the literature, carbonaceous materials were often used as the support of Ru based catalyst for the proposed reaction. For instance, Ru supported on synthesized N-doped carbon nanoflakes was used as the catalyst for LA to GVL conversion in the presence of formic acid as the hydrogen donor and water as the solvent. It was demonstrated that the high Ru nanoparticles dispersion on N-doped carbon guaranteed a high activity of the catalyst giving 99.8% LA conversion and 100% selectivity of GVL at 140 °C after 20 h [63]. Carbon supported Ni was also used as the catalyst in some studies. For example, commercial activated carbon was applied as the Ni support (Ni/AC) in which 99 % GVL selectivity at 80 % LA conversion was achieved using dioxane as the solvent at 200 °C and 30 bar H_2, for 4 h [21]. A recent study reported melamine as an N-doped carbonaceous support and introduced Al and Ni via coprecipitation method [64]. The authors suggested that N-doped carbon assisted creation of NiNx species and hence a high activity of the catalyst. A similar result to current study was obtained (LA conversion of 96 % and GVL yield of 94 %) at 130 °C, 10 bar H_2 and 3 h reaction time [64]. Indeed, in our study, the A_T activated biochar in NiAlp/A_T, as one of the best catalysts, had a high amount of nitrogen heteroatom in the structure which could be both doped and functionalized groups as confirmed by XPS in one of our recent publication for a different application [4]. This can be an advantage to use a self-doped carbonaceous material from wastes and use it for a catalytic application. In the next section, the optimization of the reaction conditions over NiAlp/A_W as one of the best catalyst will be discussed.

3.5. *Optimization of the reaction conditions over NiAlp/A_W catalyst*

A series of catalytic runs were carried out to study the effect of reaction conditions such as temperature, H_2 pressure, time, and LA/catalyst mass ratio on the reactivity and finally to select the optimum condition for GVL production. NiAlp/A_W was selected for this investigation because it was one of the most active catalysts in the screening step. The increase of the reaction temperature from 150 °C to 180 °C increased the LA conversion from 69 % to 92 %, and GVL yield from 62 % to 88 %, respectively (Fig. 11a). However, a further increase of the temperature to 200 °C did not show a sharp difference in LA conversion and GVL yield. Subsequently, 180 °C was selected as the reaction temperature for further investigation as temperature higher than 200 °C might lead to formation of degradation compounds such as humins which was confirmed by a decrease of the CB from 97 % to 94 %, respectively. By enhancing the H_2 pressure from 15 bar to 25 bar, the LA conversion and GVL were remarkably raised, and from 25 bar to 35 bar, the LA conversion stayed almost similar but GVL yield slightly increased

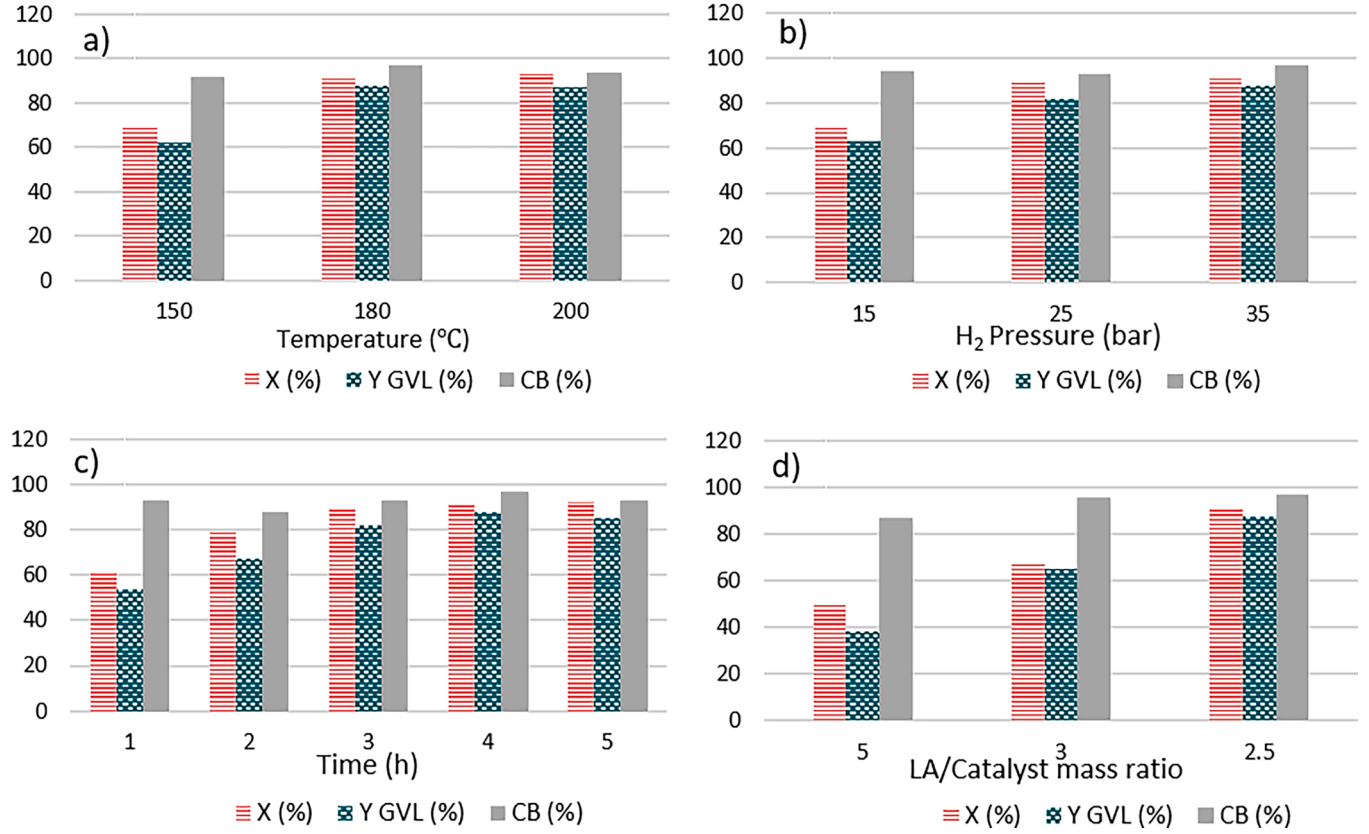

Fig. 11. Hydrogenation of LA over NiAlp/A_W catalyst (a) at different temperatures. (Reaction conditions: 35 bar H_2, 4 h, 0.17 M LA, 400 mg catalyst, 50 ml H_2O), (b) at different H_2 pressures. (Reaction conditions: 180 °C, 4 h, 0.17 M LA, 400 mg catalyst, 50 ml H_2O), (c) at different reaction times. (Reaction conditions: 180 °C, 35 bar H_2, 0.17 M LA, 400 mg catalyst, 50 ml H_2O), and (d) at different LA/catalyst mass ratios. (Reaction conditions: 180 °C, 35 bar H_2, 4 h, 50 ml H_2O). The relative error of HPLC analysis was generally less than ± 5 %.

(Fig. 11b). Therefore, 35 bar of H_2 was selected for the experiments with different reaction times and LA/catalyst mass ratios. Increasing the reaction time from 1 h to 3 h resulted in a significant increase of LA conversion and GVL yield (Fig. 11c). Finally, it reached up to the maximum GVL yield after 4 h. However, further prolonging of reaction time did not significantly affect the LA conversion but decreased GVL yield which might be due to the occurrence of side reactions and production of solid residues such as coke and humins being explained by decreasing CB from 97 % to 93 %, respectively. Finally, the increase of LA/catalyst mass ratio resulted in a decrease of catalytic activity (Fig. 11d). It is shown that the LA/catalyst mass ratio of 2.5 was the optimum value for the proposed catalytic reaction (nNi/nLA=0.08). Liu et al., reported%99 GVL selectivity over N-doped multichambered mesoporous carbon microspheres supported Ni catalysts (Ni@NCMs) with nNi/nLA of 0.04 [21], whereas Obregón and co-workers produced 91 % yield of GVL using Ni/Al_2O_3 catalyst with nNi/nLA of 1.4 [16].

Overall, when optimizing the reaction conditions, no byproduct was detected in the liquid phase by HPLC and GC/MS analyses. Hence, we assumed that the byproduct might be in solid phase depositing on the catalysts surface which was also confirmed by reducing CB value. Interestingly, even at softest reaction conditions of this study, the catalyst showed a reasonable productivity being a promising factor in catalytic application.

4. Conclusions

Activated biochar was synthesized as a sustainable and efficient carbonaceous support for bifunctional Ni, Al-catalysts in hydrogenation reactions. A comparative investigation among different activated biochars obtained from pyrolysis and CO_2-based activation of leather tannery waste, vine wood waste, barley waste, and Venice lagoon brown algae suggested that the chemical, textural and morphological properties of activated biochars are highly affected by the origin of the initial biomasses. CHNS elemental analysis showed a higher carbon fraction for A_T and A_W confirming their higher aromaticity and stability as catalyst supports. In addition, the highest nitrogen amount for A_T and A_B, and oxygen amount for A_W confirmed higher amounts of N,O-doped and functional groups of the carbon-based supports, as it was also observed in FTIR and TPD results, being suitable for introduction and anchorage of active metal sites. According to N_2 physisorption, the porous textures and high surface areas of all supports were successfully achieved through activation procedure except for the A_B due to a different origin of initial B biomass which required harsher activation conditions. The weak porosity and low surface area of A_B and the existence of poisoning sulfur in A_A were the main reasons for the low activity of the catalysts. Hence, A_T and A_W acted as the best supports of the catalyst allowing better dispersion of the active phases (XRD and TEM results) and subsequently highest activity in LA conversion to GVL as a model hydrogenation reaction. Al-containing species as the Lewis acid sites were introduced by impregnation and precipitation. Precipitation technique could better improve weak Lewis acid site dispersion and its better activity in dehydration step of the reaction. Among all catalysts, NiAlp/A_T and NiAlp/A_W acted as the best ones producing ca. 95 % LA conversion and GVL yield and TOF of ca. $95^{*}10^{-5}$ s^{-1} at 200 °C, under 35 bar H_2, after 4 h in an aqueous medium. The result of this study proves that not only the selection of different types of biomasses from animal and vegetal origins could result in different properties of derived biochar based supports, but also with biochar post-treatment approaches such as activations and functionalization, the desired textural, morphological and chemical properties could be modified for catalytic application.

Author contributions

For transparency, we require corresponding authors to provide co-author contributions to the manuscript using the relevant CRediT roles. The CRediT taxonomy includes 14 different roles describing each contributor's specific contribution to the scholarly output. The roles are: Conceptualization; Data curation; Formal analysis; Funding acquisition; Investigation; Methodology; Project administration; Resources; Software; Supervision; Validation; Visualization; Roles/Writing - original draft; and Writing - review & editing. Note that not all roles may apply to every manuscript, and authors may have contributed through multiple roles

Declaration of Competing Interest

The authors declare that they have no known competing financial interests or personal relationships that could have appeared to influence the work reported in this paper.

Data availability

Data will be made available on request.

Acknowledgments

MIUR (Italian Ministry for Education, University and Research) is kindly acknowledged for the doctoral scholarship of the inter-university PhD program of Trieste University and Ca' Foscari University of Venice. Conceria Pasubio S.p.A is acknowledged for supplying leather shaving waste. Mr. Sebastiano Tieuli and Miss Martina Tretti are acknowledged for some technical analyses.

Supplementary materials

Supplementary material associated with this article can be found, in the online version, at doi:10.1016/j.cartre.2023.100316.

References

[1] G. Michelini, R.N. Moraes, R.N. Cunha, J.M.H. Costa, A.R. Ometto, From linear to circular economy: PSS conducting the transition, Procedia CIRP 64 (2017) 2–6, https://doi.org/10.1016/J.PROCIR.2017.03.012.
[2] O. Norouzi, S. Taghavi, P. Arku, S. Jafarian, M. Signoretto, A. Dutta, What is the best catalyst for biomass pyrolysis? J. Anal. Appl. Pyrolysis 158 (2021), 105280 https://doi.org/10.1016/J.JAAP.2021.105280.
[3] G. Ferraro, G. Pecori, L. Rosi, L. Bettucci, E. Fratini, D. Casini, A.M. Rizzo, D. Chiaramonti, Biochar from lab-scale pyrolysis: influence of feedstock and operational temperature, Biomass Convers. Biorefin. (2022) 1–11, https://doi.org/10.1007/S13399-021-01303-5.
[4] P. Salimi, S. Tieuli, S. Taghavi, E. Venezia, S. Fugattini, S. Lauciello, M. Prato, S. Marras, T. Li, M. Signoretto, P. Costamagna, R.Proietti Zaccaria, Sustainable lithium-ion batteries based on metal-free tannery waste biochar, Green Chem. 24 (2022) 4119–4129, https://doi.org/10.1039/D1GC04772H.
[5] K. Qian, A. Kumar, H. Zhang, D. Bellmer, R. Huhnke, Recent advances in utilization of biochar, Renew. Sustain. Energy Rev. 42 (2015) 1055–1064, https://doi.org/10.1016/J.RSER.2014.10.074.
[6] P. Salimi, E. Venezia, S. Taghavi, S. Tieuli, L. Carbone, M. Prato, M. Signoretto, J. Qiu, R.P. Zaccaria, Lithium-metal free sulphur battery based on waste biomass anode and nano-sized Li2S cathode, Energy Environ. Mater. (2022) e12567, https://doi.org/10.1002/EEM2.12567.
[7] Y. Yang, Y. Piao, R. Wang, Y. Su, N. Liu, Y. Lei, Nonmetal function groups of biochar for pollutants removal: a review, J. Hazard. Mater. Adv. 8 (2022), 100171, https://doi.org/10.1016/J.HAZADV.2022.100171.
[8] J. Xi, H. Li, J. Xi, S. Tan, J. Zheng, Z. Tan, Preparation of high porosity biochar materials by template method: a review, Environ. Sci. Pollut. Res. 27 (2020) 20675–20684, https://doi.org/10.1007/s11356-020-08593-8.
[9] A.K. Sakhiya, P. Baghel, A. Anand, V.K. Vijay, P. Kaushal, A comparative study of physical and chemical activation of rice straw derived biochar to enhance Zn+2 adsorption, Bioresour. Technol. Rep. 15 (2021), 100774, https://doi.org/10.1016/J.BITEB.2021.100774.
[10] B. Notarnicola, R. Puig Vidal, A. Raggi, P. Fullana Palmer, G. Tassielli, C. de Camillis, A. Rius Carrasco, Life cycle assessment of Italian and Spanish bovine leather production systems, Afinidad Rev. Quím. Teór. Apl. 68 (2011) 167–180. https://upcommons.upc.edu/handle/2117/14093 (accessed August 19, 2023).
[11] S. Taghavi, O. Norouzi, A. Tavasoli, F. Di Maria, M. Signoretto, F. Menegazzo, A. Di Michele, Catalytic conversion of Venice lagoon brown marine algae for producing hydrogen-rich gas and valuable biochemical using algal biochar and Ni/SBA-15 catalyst, Int. J. Hydrog. Energy 43 (2018) 19918–19929, https://doi.org/10.1016/J.IJHYDENE.2018.09.028.

[12] F. Kerkel, M. Markiewicz, S. Stolte, E. Müller, W. Kunz, The green platform molecule gamma-valerolactone – ecotoxicity, biodegradability, solvent properties, and potential applications, Green Chem. 23 (2021) 2962–2976, https://doi.org/10.1039/D0GC04353B.
[13] Z. Zhang, Synthesis of γ-valerolactone from carbohydrates and its applications, ChemSusChem 9 (2016) 156–171, https://doi.org/10.1002/CSSC.201501089.
[14] Z. Yu, X. Lu, H. Bai, J. Xiong, W. Feng, N. Ji, Effects of solid acid supports on the bifunctional catalysis of levulinic acid to γ-valerolactone: catalytic activity and stability, Chem. Asian J. 15 (2020) 1182–1201, https://doi.org/10.1002/ASIA.202000006.
[15] S. Dutta, I.K.M. Yu, D.C.W. Tsang, Y.H. Ng, Y.S. Ok, J. Sherwood, J.H. Clark, Green synthesis of gamma-valerolactone (GVL) through hydrogenation of biomass-derived levulinic acid using non-noble metal catalysts: a critical review, Chem. Eng. J. 372 (2019) 992–1006, https://doi.org/10.1016/J.CEJ.2019.04.199.
[16] I. Obregón, E. Corro, U. Izquierdo, J. Requies, P.L. Arias, Levulinic acid hydrogenolysis on Al_2O_3-based Ni-Cu bimetallic catalysts, Chin. J. Catal. 35 (2014) 656–662, https://doi.org/10.1016/S1872-2067(14)60051-6.
[17] M. Chia, J.A. Dumesic, Liquid-phase catalytic transfer hydrogenation and cyclization of levulinic acid and its esters to γ-valerolactone over metal oxide catalysts, Chem. Commun. 47 (2011) 12233–12235, https://doi.org/10.1039/C1CC14748J.
[18] W. Luo, U. Deka, A.M. Beale, E.R.H. Van Eck, P.C.A. Bruijnincx, B.M. Weckhuysen, Ruthenium-catalyzed hydrogenation of levulinic acid: influence of the support and solvent on catalyst selectivity and stability, J. Catal. 301 (2013) 175–186, https://doi.org/10.1016/J.JCAT.2013.02.003.
[19] L. Zhang, J. Mao, S. Li, J. Yin, X. Sun, X. Guo, C. Song, J. Zhou, Hydrogenation of levulinic acid into gamma-valerolactone over *in situ* reduced CuAg bimetallic catalyst: strategy and mechanism of preventing Cu leaching, Appl. Catal. B 232 (2018) 1–10, https://doi.org/10.1016/J.APCATB.2018.03.033.
[20] W. Cao, W. Luo, H. Ge, Y. Su, A. Wang, T. Zhang, UiO-66 derived Ru/ZrO_2@C as a highly stable catalyst for hydrogenation of levulinic acid to γ-valerolactone, Green Chem. 19 (2017) 2201–2211, https://doi.org/10.1039/C7GC00512A.
[21] D. Liu, L. Zhang, W. Han, M. Tang, L. Zhou, Y. Zhang, X. Li, Z. Qin, H. Yang, One-step fabrication of Ni-embedded hierarchically-porous carbon microspheres for levulinic acid hydrogenation, Chem. Eng. J. 369 (2019) 386–393, https://doi.org/10.1016/J.CEJ.2019.03.072.
[22] L. Longo, S. Taghavi, E. Ghedini, F. Menegazzo, A. Di Michele, G. Cruciani, M. Signoretto, Selective hydrogenation of 5-hydroxymethylfurfural to 1-hydroxy-2,5-hexanedione by biochar-supported Ru catalysts, ChemSusChem 15 (2022), e202200437, https://doi.org/10.1002/CSSC.202200437.
[23] L. Longo, S. Taghavi, M. Riello, E. Ghedini, F. Menegazzo, A. Di Michele, G. Cruciani, M. Signoretto, Waste biomasses as precursors of catalytic supports in benzaldehyde hydrogenation, Catal. Today 420 (2023), 114038, https://doi.org/10.1016/J.CATTOD.2023.02.015.
[24] S. Jafarian, A.M.L. Bolouk, R. Norouzian, S. Taghavi, F. Mousavi, E. Kianpour, M. Signoretto, Sargassum macro-algae-derived activated bio-char as a sustainable and cost-effective adsorbent for cationic dyes: a joint experimental and DFT study, Colloids Surf. A Physicochem. Eng. Asp. 678 (2023), 132397, https://doi.org/10.1016/J.COLSURFA.2023.132397.
[25] R. Ramos, V.K. Abdelkader-fernández, R. Matos, A.F. Peixoto, D.M. Fernandes, Metal-supported biochar catalysts for sustainable biorefinery, electrocatalysis, and energy storage applications: a review, Catalysts 12 (2022) 207, https://doi.org/10.3390/CATAL12020207.
[26] Standard test methods for proximate analysis of coal and coke by macro thermogravimetric analysis, ASTM D7582-15 (2023). https://www.astm.org/d7582-15.html.
[27] P.H. Emmett, S. Brunauer, The use of low temperature van der Waals adsorption isotherms in determining the surface area of iron synthetic ammonia catalysts, J. Am. Chem. Soc. 59 (1937) 1553–1564, https://doi.org/10.1021/ja01287a041.
[28] D. Angin, Effect of pyrolysis temperature and heating rate on biochar obtained from pyrolysis of safflower seed press cake, Bioresour. Technol. 128 (2013) 593–597, https://doi.org/10.1016/J.BIORTECH.2012.10.150.
[29] P.S. Thue, D.R. Lima, E.C. Lima, R.A. Teixeira, G.S. Dos Reis, S.L.P. Dias, F. M. Machado, Comparative studies of physicochemical and adsorptive properties of biochar materials from biomass using different zinc salts as activating agents, J. Environ. Chem. Eng. 10 (2022), 107632, https://doi.org/10.1016/J.JECE.2022.107632.
[30] H.S. Jatav, V.D. Rajput, T. Minkina, S.K. Singh, S. Chejara, A. Gorovtsov, A. Barakhov, T. Bauer, S. Sushkova, S. Mandzieva, M. Burachevskaya, V. P. Kalinitchenko, Sustainable approach and safe use of biochar and its possible consequences, Sustainability 13 (2021) 10362, https://doi.org/10.3390/SU131810362.
[31] H. Shan, X. Li, Y. Cui, D. Xiong, B. Yan, D. Li, A. Lushington, X. Sun, Sulfur/nitrogen dual-doped porous graphene aerogels enhancing anode performance of lithium ion batteries, Electrochim. Acta 205 (2016) 188–197, https://doi.org/10.1016/J.ELECTACTA.2016.04.105.
[32] S. De, J. Zhang, R. Luque, N. Yan, Ni-based bimetallic heterogeneous catalysts for energy and environmental applications, Energy Environ. Sci. 9 (2016) 3314–3347, https://doi.org/10.1039/C6EE02002J.
[33] C.H. Bartholomew, G.D. Weatherbee, G.A. Jarvi, Sulfur poisoning of nickel methanation catalysts: I. *In situ* deactivation by H_2S of nickel and nickel bimetallics, J. Catal. 60 (1979) 257–269, https://doi.org/10.1016/0021-9517(79)90147-7.
[34] A. Kolpin, G. Jones, S. Jones, W. Zheng, J. Cookson, A.P.E. York, P.J. Collier, S.C. E. Tsang, Quantitative differences in sulfur poisoning phenomena over ruthenium and palladium: an attempt to deconvolute geometric and electronic poisoning effects using model catalysts, ACS Catal. 7 (2017) 592–605, https://doi.org/10.1021/ACSCATAL.6B02765/ASSET/IMAGES/CS-2016-027653_M001.GIF.
[35] E. Ghedini, S. Taghavi, F. Menegazzo, M. Signoretto, A review on the efficient catalysts for algae transesterification to biodiesel, Sustainability 13 (2021) 10479, https://doi.org/10.3390/SU131810479.
[36] L. Liu, Y. Liu, W. Wang, Y. Wang, G. Li, C. Hu, Pyrolysis of high-ash natural microalgae from water blooms: effects of acid pretreatment, Toxins 13 (2021) 542, https://doi.org/10.3390/TOXINS13080542/S1 (Basel).
[37] W.T. Tsai, T.J. Jiang, Y.Q. Lin, H.L. Chang, C.H. Tsai, Preparation of porous biochar from soapberry pericarp at severe carbonization conditions, Fermentation 7 (2021) 228, https://doi.org/10.3390/FERMENTATION7040228.
[38] A. Makalesi, /Research, A N. Kaya, Z. Yildiz, S. Ceylan, Preparation and characterisation of biochar from hazelnut shell and its adsorption properties for methylene blue dye, Politek. Derg. 21 (2018) 765–776, https://doi.org/10.2339/POLITEKNIK.386963.
[39] J.M. de la Rosa, M. Paneque, A.Z. Miller, H. Knicker, Relating physical and chemical properties of four different biochars and their application rate to biomass production of Lolium perenne on a Calcic Cambisol during a pot experiment of 79 days, Sci. Total Environ. 499 (2014) 175–184, https://doi.org/10.1016/J.SCITOTENV.2014.08.025.
[40] B. Ma, Y. Huang, Z. Nie, X. Qiu, D. Su, G. Wang, J. Yuan, X. Xie, Z. Wu, Facile synthesis of Camellia oleifera shell-derived hard carbon as an anode material for lithium-ion batteries, RSC Adv. 9 (2019) 20424–20431, https://doi.org/10.1039/C9RA03345A.
[41] Y. Liu, Z. He, M. Uchimiya, Comparison of biochar formation from various agricultural by-products using FTIR spectroscopy, Mod. Appl. Sci. 9 (2015), https://doi.org/10.5539/mas.v9n4p246.
[42] S. Javadian, Z. Parviz, P. Salimi, M. Nasrollahpour, H. Gharibi, H. Kashani, A. Morsali, R.P. Zaccaria, Engineering cobalt-based nanoparticles encapsulated in hierarchical porous N-doped carbon as an efficient electrode for Li storage, J. Alloy. Compd. 898 (2022), 162849, https://doi.org/10.1016/J.JALLCOM.2021.162849.
[43] M. González-Castaño, C. Morales, J.C. Navarro de Miguel, J.H. Boelte, O. Klepel, J. I. Flege, H. Arellano-García, Are Ni/and Ni_5Fe_1/biochar catalysts suitable for synthetic natural gas production? A comparison with γ-Al_2O_3 supported catalysts, Green Energy Environ. 8 (2021) 744–756, https://doi.org/10.1016/J.GEE.2021.05.007.
[44] I.K.M. Yu, X. Xiong, D.C.W. Tsang, L. Wang, A.J. Hunt, H. Song, J. Shang, Y.S. Ok, C.S. Poon, Aluminium-biochar composites as sustainable heterogeneous catalysts for glucose isomerisation in a biorefinery, Green Chem. 21 (2019) 1267–1281, https://doi.org/10.1039/C8GC02466A.
[45] L. Qian, B. Chen, Interactions of aluminum with biochars and oxidized biochars: implications for the biochar aging process, J. Agric. Food Chem. 62 (2014) 373–380, https://doi.org/10.1021/JF404624H/SUPPL_FILE/JF404624H_SI_001.PDF.
[46] H.K.D. Nguyen, V.V. Pham, H.T. Do, Preparation of Ni/biochar catalyst for hydrotreating of bio-oil from microalgae biomass, Catal. Lett. 146 (2016) 2381–2391, https://doi.org/10.1007/S10562-016-1873-8/TABLES/5.
[47] T.H. Liou, S.J. Wu, Characteristics of microporous/mesoporous carbons prepared from rice husk under base- and acid-treated conditions, J. Hazard. Mater. 171 (2009) 693–703, https://doi.org/10.1016/J.JHAZMAT.2009.06.056.
[48] M.M. Alam, M.A. Hossain, M.D. Hossain, M.A.H. Johir, J. Hossen, M.S. Rahman, J. L. Zhou, A.T.M.K. Hasan, A.K. Karmakar, M.B. Ahmed, The potentiality of rice husk-derived activated carbon: from synthesis to application, Processes 8 (2020) 203, https://doi.org/10.3390/PR8020203.
[49] X. Liu, Y. Zhang, M.A. Nahil, P.T. Williams, C. Wu, Development of Ni- and Fe-based catalysts with different metal particle sizes for the production of carbon nanotubes and hydrogen from thermo-chemical conversion of waste plastics, J. Anal. Appl. Pyrolysis 125 (2017) 32–39, https://doi.org/10.1016/J.JAAP.2017.05.001.
[50] Q. Yin, H. Ren, R. Wang, Z. Zhao, Evaluation of nitrate and phosphate adsorption on Al-modified biochar: influence of Al content, Sci. Total Environ. 631–632 (2018) 895–903, https://doi.org/10.1016/J.SCITOTENV.2018.03.091.
[51] K. Hengst, D.A.J.M. Ligthart, D.E. Doronkin, K.M. Walter, W. Kleist, E.J.M. Hensen, J.D. Grunwaldt, Continuous synthesis of γ-valerolactone in a trickle-bed reactor over supported nickel catalysts, Ind. Eng. Chem. Res. 56 (2017) 2680–2689, https://doi.org/10.1021/ACS.IECR.6B03493/ASSET/IMAGES/LARGE/IE-2016-03493H_0009.JPEG.
[52] M. Wolf, C. Schüler, O. Hinrichsen, Sulfur poisoning of co-precipitated Ni–Al catalysts for the methanation of CO_2, J. CO2 Util. 32 (2019) 80–91, https://doi.org/10.1016/J.JCOU.2019.03.003.
[53] J.M.V. Nabais, C. Laginhas, P.J.M. Carrott, M.M.L.R. Carrott, Thermal conversion of a novel biomass agricultural residue (vine shoots) into activated carbon using activation with CO2, J. Anal. Appl. Pyrolysis 87 (2010) 8–13, https://doi.org/10.1016/J.JAAP.2009.09.004.
[54] J.L. Santos, P. Mäki-Arvela, A. Monzón, D.Y. Murzin, M.Á. Centeno, Metal catalysts supported on biochars: part I synthesis and characterization, Appl. Catal. B 268 (2020), 118423, https://doi.org/10.1016/J.APCATB.2019.118423.
[55] Y. Wang, Z. Zhang, S. Zhang, Y. Wang, S. Hu, J. Xiang, X. Hu, Steam reforming of acetic acid over Ni/biochar catalyst treated with HNO_3: impacts of the treatment on surface properties and catalytic behaviors, Fuel 278 (2020), 118341, https://doi.org/10.1016/J.FUEL.2020.118341.
[56] C. Quan, H. Wang, N. Gao, Development of activated biochar supported Ni catalyst for enhancing toluene steam reforming, Int. J. Energy Res. 44 (2020) 5749–5764, https://doi.org/10.1002/ER.5335.

[57] J.M. Rafi, A. Rajashekar, M. Srinivas, B.V.S.K. Rao, R.B.N. Prasad, N. Lingaiah, Esterification of glycerol over a solid acid biochar catalyst derived from waste biomass, RSC Adv. 5 (2015) 44550–44556, https://doi.org/10.1039/C5RA06613A.

[58] D.M. Alonso, J.M.R. Gallo, M.A. Mellmer, S.G. Wettstein, J.A. Dumesic, Direct conversion of cellulose to levulinic acid and gamma-valerolactone using solid acid catalysts, Catal. Sci. Technol. 3 (2013) 927–931, https://doi.org/10.1039/C2CY20689G.

[59] C. Moreno-Marrodan, P. Barbaro, Energy efficient continuous production of γ-valerolactone by bifunctional metal/acid catalysis in one pot, Green Chem. 16 (2014) 3434–3438, https://doi.org/10.1039/C4GC00298A.

[60] V.V. Kumar, G. Naresh, M. Sudhakar, J. Tardio, S.K. Bhargava, A. Venugopal, Role of Brønsted and Lewis acid sites on Ni/TiO_2 catalyst for vapour phase hydrogenation of levulinic acid: kinetic and mechanistic study, Appl. Catal. A Gen. 505 (2015) 217–223, https://doi.org/10.1016/J.APCATA.2015.07.031.

[61] C. López-Aguado, M. Paniagua, J.A. Melero, J. Iglesias, P. Juárez, M.L. Granados, G. Morales, Stable continuous production of γ-valerolactone from biomass-derived levulinic acid over Zr–Al-beta zeolite catalyst, Catalysts 10 (2020) 678, https://doi.org/10.3390/CATAL10060678.

[62] S.L. Lakhapatri, M.A. Abraham, Sulfur poisoning of Rh–Ni catalysts during steam reforming of sulfur-containing liquid fuels, Catal. Sci. Technol. 3 (2013) 2755–2760, https://doi.org/10.1039/C3CY00351E.

[63] A. Chauhan, A.K. Kar, R. Srivastava, Ru-decorated N-doped carbon nanoflakes for selective hydrogenation of levulinic acid to γ-valerolactone and quinoline to tetrahydroquinoline with HCOOH in water, Appl. Catal. A Gen. 636 (2022), 118580, https://doi.org/10.1016/J.APCATA.2022.118580.

[64] L. Jiang, G. Xu, Y. Fu, A nitrogen-doped carbon modified nickel catalyst for the hydrogenation of levulinic acid under mild conditions, Green Chem. 23 (2021) 7065–7073, https://doi.org/10.1039/D1GC01732B.